POLITECNICO
MILANO 1863

SCUOLA DI INGEGNERIA INDUSTRIALE
E DELL'INFORMAZIONE

Predictive Control with Online Jacobian Update for Dynamic Mitral Valve Targeting in Continuum Robots

Tesi di Laurea Magistrale in
Biomedical Engineering - Ingegneria Biomedica

Filippo Manini, 251210

Advisor:
Prof. Elena De Momi

Co-advisors:
Anna Bicchi

Academic year:
2024-2025

Abstract: Transcatheter mitral valve repair requires accurate targeting of anatomical structures undergoing significant physiological motion, challenging conventional control strategies based on static assumptions. This work presents a predictive control framework for dynamic target reaching with tendon-driven continuum robotic catheters.
Target motion is modeled and predicted online, and a Model Predictive Trajectory Planning (MPTP) scheme generates anticipatory trajectories toward the moving valve. To cope with the nonlinear and configuration-dependent behavior of continuum robots, an online Jacobian adaptation strategy is integrated within the control loop, augmented by dead-zone detection and motor saturation handling to ensure stability under actuation constraints.
The approach is validated on a dedicated experimental platform featuring a motorized tendon-driven continuum robot and a motion stage reproducing physiologically inspired valve dynamics. Experimental results demonstrate a success rate of 100%, outperforming classical Model Predictive Control (MPC) (55%) and analytical Proportional-Integral-Derivative (PID) (75%) baselines. The proposed method achieves shorter trajectories (72 ± 6 mm) and reduced time-to-target (260 ± 45 s), while preserving robustness across varying motion amplitudes and frequencies. These findings highlight the effectiveness of combining predictive planning with online kinematic adaptation for robotic interventions involving dynamic anatomical targets.

Key-words: Autonomous Transcatheter Mitral Valve Repair,Model Predictive Trajectory Planning, Dynamic Mitral Valve Targeting, Online Jacobian Update

1. Introduction

CardioVascular Diseases (CVDs) represent the leading cause of mortality worldwide. According to the World Health Organization , they account for approximately 32% of all global deaths [1]. In addition to their high mortality rate, CVDs significantly impair quality of Life (QoL) and impose a substantial economic burden on healthcare systems. On a global scale, their annual economic impact is estimated to be approximately 210 billion euros [2].
Nearly 30% of CVD cases are imputable to structural heart diseases (SHDs), which encompass conditions related to abnormalities of the heart valves, cardiac walls, and myocardial structures [3]. Among SHDs, Mitral

Regurgitation (MVR) is the second most prevalent valvular heart disease requiring invasive treatment in Western countries [4]. It is estimated that approximately 1.7% of the general population in the United States is affected by MR [5]. Moreover, the incidence of MR has been steadily increasing due to the progressive aging of the global population, with reported annual mortality rates approaching 34% [6–8].

1.1. Mitral Valve Anatomy

The MV is a complex anatomical structure involved in the high-pressure systemic circulation, ensuring unidirectional blood flow from the left atrium to the left ventricle (LV) [9]. The mitral valve function depends on the proper structural and functional integrity of its main components. These include the mitral annulus, the anterior and posterior leaflets, the anterolateral and posteromedial commissures (AC and PC), the chordae tendineae, and the papillary muscles, as illustrated in Fig. 1. The coordinated interaction of these structures is essential for the correct fulfillment of valve function.
The mitral annulus is a fibromuscular ring with a characteristic saddle-shaped geometry that serves as the anchoring structure for the mitral leaflets. The papillary muscles originate from the LV myocardium and are connected to the valve leaflets through the chordae tendineae. Three distinct chordal orders can be identified: primary chordae, which attach to the free edges of the leaflets and prevent leaflet prolapse into the atrium during systole; secondary and tertiary chordae, which distribute systolic loads and connect the leaflets to the ventricular wall.
The anterior leaflet is anchored to the fibrous portion of the annulus and is continuous with the aortic annulus. It is typically larger, longer, and thicker than the posterior leaflet, while exhibiting a shorter radial extension. Conversely, the posterior leaflet presents a broader annular attachment and is commonly divided by two indentations (clefts) into three scallops according to Carpentier's classification: the posterolateral scallop (P1), adjacent to the anterolateral commissure; the central scallop (P2); and the posteromedial scallop (P3), located near the posteromedial commissure [5]. The corresponding regions of the anterior leaflet are referred to as A1, A2, and A3, respectively [9]. These anatomical landmarks are routinely used as reference points during clinical interventions on the mitral valve.
Additional relevant anatomical structures surrounding the mitral annulus include the circumflex coronary artery, which courses along the left portion of the mural leaflet, and the coronary sinus, located adjacent to its right portion [10]. Alterations or pathological conditions affecting the anatomical or functional integrity of any of these components may result in significant physiological impairment, including the development of Mitral Valve Regurgitation (MVR).

1.2. Mitral Valve Regurgitation (MVR)

MVR is a pathological condition in which the mitral valve fails to achieve complete closure during left ventricular systole, allowing retrograde blood flow from the Left Ventricle (LV) into the left atrium, which represents an abnormal hemodynamic direction. As illustrated in Fig. 2, the integrity and competence of the MV apparatus can be compromised by several factors, among which mitral valve prolapse, chordae tendineae rupture, and annular dilatation are the most prevalent.
MVR can be classified as either primary (degenerative) or secondary (functional) in nature [11]. Primary MVR arises from structural abnormalities of the valve apparatus components themselves, whereas secondary MVR is caused by functional alterations of otherwise anatomically normal valve structures. In the latter case, pathological remodeling of the LV often results in leaflet tethering, defined as the restricted motion of the valve leaflets due to LV dilatation and an increased ventricular sphericity index. These changes induce apical displacement of the papillary muscles and lateral displacement of the leaflet closing forces, ultimately leading to incomplete leaflet coaptation and the onset of MVR.
The clinical presentation of MVR can be further categorized as acute or chronic. Acute MVR, also referred to as sudden MVR, is typically caused by abrupt disruption of the valve's mechanical integrity. Representative etiologies include leaflet vegetations associated with infective endocarditis, chordae tendineae rupture in patients with pre-existing degenerative disease, and papillary muscle rupture. In such cases, the sudden volume overload imposed on the left atrium exceeds its compensatory capacity, resulting in rapid elevation of atrial and pulmonary pressures. Consequently, patients may develop acute dyspnea due to pulmonary congestion, requiring immediate clinical intervention [9].
Chronic MVR, on the other hand, develops progressively and may be associated with either primary or secondary mechanisms. In chronic primary MVR, leaflet degeneration—most commonly due to myxomatous disease—prevents proper leaflet coaptation, often resulting in prolapse. In chronic secondary MVR, the valve leaflets remain structurally normal, but their function is impaired by LV pathology. This impairment may be caused by annular dilatation secondary to LV enlargement, which prevents effective leaflet apposition, or by

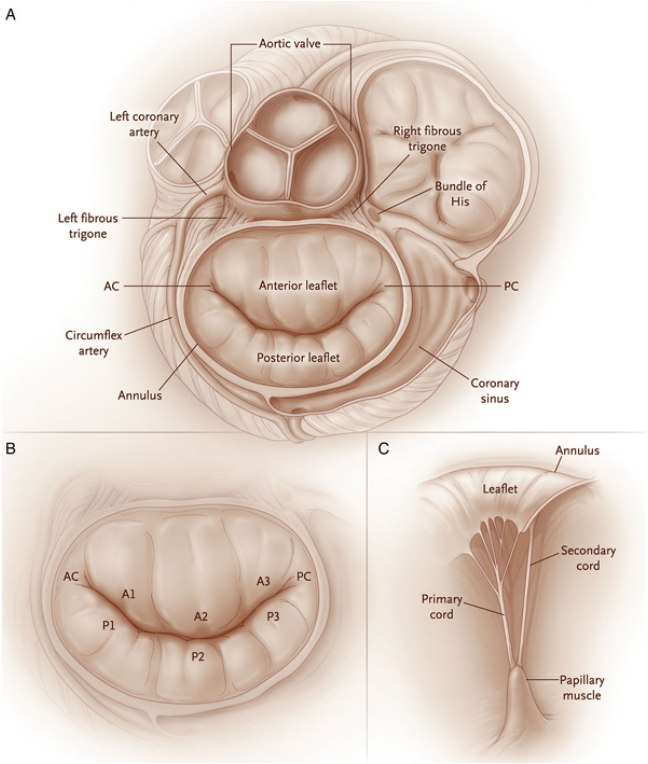

Figure 1: The mitral valve and surrounding structures from different point of views. (A) Top view with the details of the close mitral valve (B); (C) Frontal view.

abnormal LV wall motion following ischemia or myocardial infarction [9]. Persistent LV volume overload leads to increased wall stress, progressive deterioration of ventricular contractility, and reduced annular closing forces, thereby exacerbating regurgitant volume.
If left untreated, significant MVR imposes a chronic hemodynamic burden on both the heart and the pulmonary circulation, potentially resulting in left atrial enlargement, atrial fibrillation, and pulmonary hypertension. These long-term complications can substantially impair cardiac efficiency, patient QoL, and life expectancy. Consequently, upon high severity of MVR, a surgical procedure is needed. In the section below the main surgical treatments are described

1.3. From mitral Valve Replacement to Mitral Valve Repair: Open-Heart Surgery vs Minimally Invasive Surgery

Surgical intervention represents the only therapeutic strategy with well-established and durable clinical efficacy for the treatment of MVR, providing long-term symptom relief and improved outcomes in patients with heart failure [4]. Two main surgical approaches are currently adopted in clinical practice: mitral valve replacement and mitral valve repair. In mitral valve replacement, the native valve is excised and substituted with a mechanical or bioprosthetic valve, a solution generally reserved for cases in which the valve apparatus is severely damaged or not amenable to repair. In contrast, mitral valve repair aims to restore the physiological function of the native valve by correcting leaflet malcoaptation, repairing chordal abnormalities, and reinforcing annular geometry, thereby preserving the integrity of the subvalvular apparatus.
Over the last decade, the number of surgical procedures for MVR has increased significantly [12]. Concurrent advancements in surgical techniques, together with an improved understanding of mitral valve anatomy and pathophysiology, have driven a progressive shift toward mitral valve repair as the preferred alternative to valve replacement. This shift has enabled the successful repair of valves affected by advanced myxomatous degeneration, which were previously considered unsuitable for reconstructive procedures [13]. Compared with valve replacement, mitral valve repair has demonstrated superior long-term survival, better preservation of left ventricular function, and a lower incidence of prosthesis-related complications, including thromboembolic events, anticoagulation-related hemorrhage, and infective endocarditis [14]. As a result, mitral valve repair is currently regarded as the optimal surgical treatment for MVR in patients with high fragilyies [14].
Mitral valve repair can be performed using either a conventional open-heart surgical approach or a minimally invasive strategy.

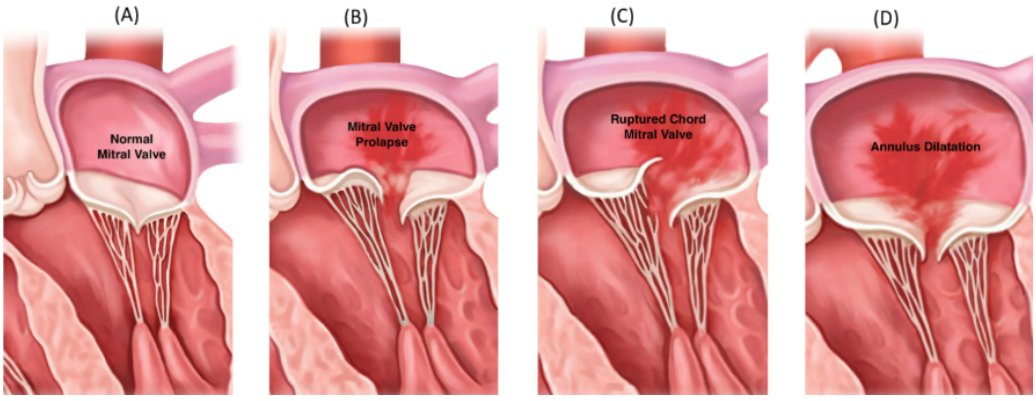

Figure 2: MVR mechanisms: (A) intact and normal left ventricular apparatus; (B) mitral valve prolapse; (C) MVR caused by chordae rupture; (D) annular dilatation leading to MVR.

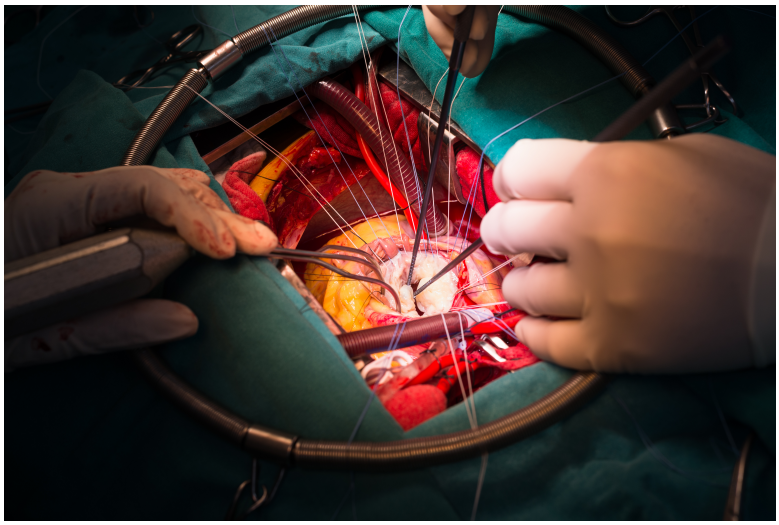

Figure 3: Conventional open-heart mitral valve repair. A median sternotomy provides direct access and visualization of the heart, allowing surgical correction of mitral valve leaflet pathology [15].

The conventional surgical approach involves a median sternotomy, consisting of a full longitudinal incision of the sternum to achieve direct exposure of the heart and mitral valve apparatus, as illustrated in Fig. 3. This approach offers excellent visualization and surgical control, facilitating complex reconstructive maneuvers on the mitral leaflets, chordae tendineae, and annulus. However, it is associated with significant surgical trauma and prolonged recovery times. Additionally, advanced age and concomitant systemic comorbidities substantially increase the physiological and immunological stress associated with open-heart surgery. In these high-risk patient populations, the invasiveness of the procedure may translate into an unacceptable perioperative risk.
Minimally invasive mitral valve surgery, on the other hand, encompasses a group of procedures performed through small thoracic incisions or percutaneous catheter-based access, without the need for full sternotomy. These techniques rely on real-time imaging guidance, such as fluoroscopy and transesophageal echocardiography, to navigate and position repair devices within the heart, as shown in Fig. 4.
The primary objective of minimally invasive approaches is to reduce surgical trauma while preserving the efficacy of conventional open-heart mitral valve repair [17]. Clinical studies have reported several advantages associated with minimally invasive mitral valve surgery, including reduced postoperative pain, lower blood loss, decreased risk of wound infection, shorter intensive care unit (ICU) stay, reduced hospital length of stay, and faster return to daily activities [18]. These benefits are clinically relevant both for improving patient QoL and for enhancing healthcare system efficiency in terms of resource utilization and overall clinical outcomes.
At present, multiple percutaneous mitral valve repair techniques are available at different stages of clinical validation. While some devices have been widely adopted in routine clinical practice and are supported by extensive clinical evidence, others remain under investigation in preclinical studies or early-phase clinical trials [19] [20], [21] ,[22].

Figure 4: Minimally invasive mitral valve repair procedure. Catheter-based devices are deployed under imaging guidance to restore leaflet coaptation without open surgical access [16].

1.4. MitraClip^{TM} System: Introduction to the system, surgical procedure and clinical limitations

The MitraClip^{TM} system represents the most widely adopted device for minimally invasive percutaneous edge-to-edge Transcatheter Mitral Valve Repair (TMVR), with over two decades of documented clinical safety and more than 200,000 patients treated worldwide [23]. The implantation of the MitraClip device replicates the surgical edge-to-edge repair originally proposed by Alfieri [24], replacing surgical sutures with a clip-based mechanism that mechanically approximates the mitral valve leaflets. The MitraClip system consists of two primary subsystems [25]: the Steerable Guide Catheter (SGC) and the Clip Delivery System (CDS), as illustrated in Fig. 5.

The Steerable Guide Catheter (SGC) enables advancement from the peripheral vascular access to the cardiac chambers. It is controlled through the Steerable Guide Handle, which provides two degrees of freedom (DoFs): (i) axial rotation about the insertion axis and (ii) bending in the medio-lateral (ML) direction via a dedicated control knob.

The Clip Delivery System (CDS) is responsible for positioning, orienting, and deploying the MitraClip device at the mitral valve level. It comprises three main components: the Delivery Catheter, the Steerable Delivery Handle, and the MitraClip implant itself.

The Delivery Catheter is actuated through two independent control knobs, allowing deflection in both the medio-lateral (ML) and antero-posterior (AP) planes (see Fig. 8). The Steerable Delivery Handle implements a triaxial tendon-driven configuration: two antagonistic tendons enable bending in the AP plane (anterior and posterior directions), while a third tendon controls bending in the ML plane toward the medial direction, i.e., toward the mitral valve.

Overall, the MitraClip delivery system provides two orientational DoFs (AP and ML bending) and one translational degree of freedom to the MitraCSlip device, associated with insertion of the Delivery Catheter within the Guide Catheter. The entire system is mechanically actuated through manual control knobs, without embedded motorization or active sensing.

At the distal end of the delivery system, the MitraClip implant consists of a cobalt-chromium device with a width ranging from 4 to 12 mm, featuring two arms and two grippers designed to securely capture the mitral valve leaflets. The opening and closing of the clip arms are controlled through mechanisms located on the CDS handle. The clip arms are covered with a polyester fabric to promote tissue ingrowth and long-term stabilization following implantation.

1.4.1. Procedure

The MitraClip procedure is performed under general anesthesia and relies on the combined use of fluoroscopy and transesophageal echocardiography (TEE), which provide real-time two-dimensional imaging essential for procedural guidance and device positioning. Vascular access is obtained through the femoral vein, from which the MitraClip delivery system is advanced into the right atrium. Following a transseptal puncture, the device is introduced into the left atrium and oriented toward the mitral valve orifice.

Once within the left atrium, the delivery is carefully steered and aligned axially with the regurgitant jet, ensuring

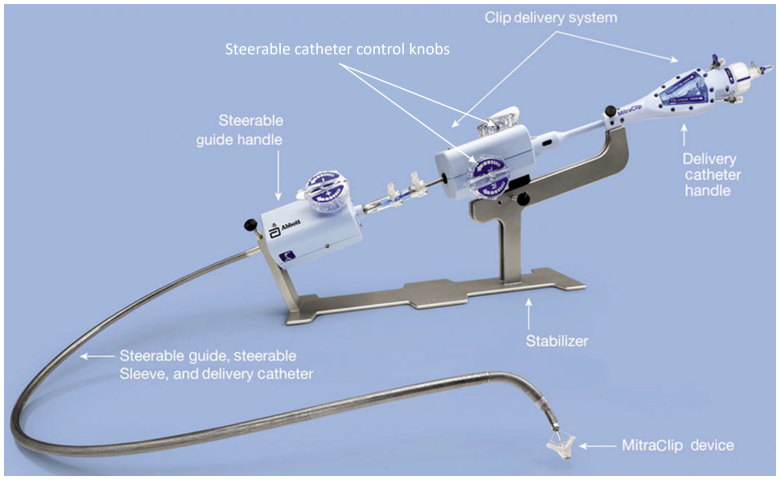

Figure 5: Overview of the MitraClip System and its components, i.e the Clip Delivery System and the Steerable Guide Catheter.The latter is in turn composed of the Delivery Catheter, the Steerable Delivery Handle and the MitraClip Device [26].

accurate positioning relative to the mitral leaflets. The clip arms are then opened and the device is advanced into the left ventricle, below the level of the mitral valve. Subsequently, the system is slowly retracted, allowing grasping of both mitral leaflets. Adequate leaflet capture and reduction of mitral regurgitation are verified using TEE imaging. Once correct positioning and satisfactory functional results are confirmed, the clip is closed and released, and the delivery catheter is withdrawn. If required, multiple clips may be implanted to achieve optimal reduction of mitral regurgitation.
Overall, the MitraClip implantation procedure can be summarized in six main steps [27], also illustrated in Fig. 6:

A. Transseptal puncture to gain access from the right atrium to the left atrium.
B. Advancement of the Clip Delivery System (CDS) toward the mitral valve.
C. Positioning and alignment of the MitraClip above the mitral valve leaflets.
D. Advancement of the CDS into the left ventricle beneath the mitral valve.
E. Grasping of the mitral valve leaflets and verification of adequate leaflet insertion within the clip.
F. Release of the clip and final assessment of procedural outcome.

1.4.2. MitraClip: strengths and limitations

The clinical efficacy of the MitraClip system has been extensively validated through numerous trials, consistently demonstrating its safety, procedural success, and positive impact on patient outcomes [28–31]. MitraClip implantation has been shown to significantly reduce MVR, improve functional capacity, and enhance the QoL. Nevertheless, the procedure remains technically demanding, requiring exceptional dexterity and precision to properly manipulate the CDS and achieve accurate alignment of the clip on the mitral leaflets. The principal challenge lies in navigating the CDS within a three-dimensional cardiac environment using only two-dimensional imaging, which is complex to interpret in real time, thereby necessitating rigorous and specific operator training [32].
Improper placement or misalignment of the clip may compromise procedural efficacy, resulting in incomplete MVR reduction or interference with valve function, potentially leading to adverse outcomes such as heart failure, stroke, or death [33]. Critical steps include steering the CDS, positioning the clip above the leaflets, grasping the leaflets, and verifying successful leaflet capture prior to release [34], all of which contribute to the steep learning curve associated with the technique [35]. Evidence suggests that operators require a minimum of 50 procedures to observe improvements in outcomes, while mastery, including enhanced technical skills and optimized heart team coordination, is generally achieved after 200 or more procedures. Another procedural risk is radiation exposure for both patients and clinical staff due to fluoroscopic guidance [36].
To address these limitations, robotic-assisted technologies have been increasingly explored in interventional cardiology. Robotics has been successfully applied in percutaneous coronary interventions and peripheral vascular interventions, demonstrating potential improvements in procedural precision, reliability, and reduction in radiation exposure. Moreover, robotic systems can mitigate occupational injuries associated with lead apron usage [37]. Studies indicate that operators achieve proficiency after as few as three robotic-assisted procedures, significantly reducing procedure time, radiation exposure, optimizing overall learning curves, and improving

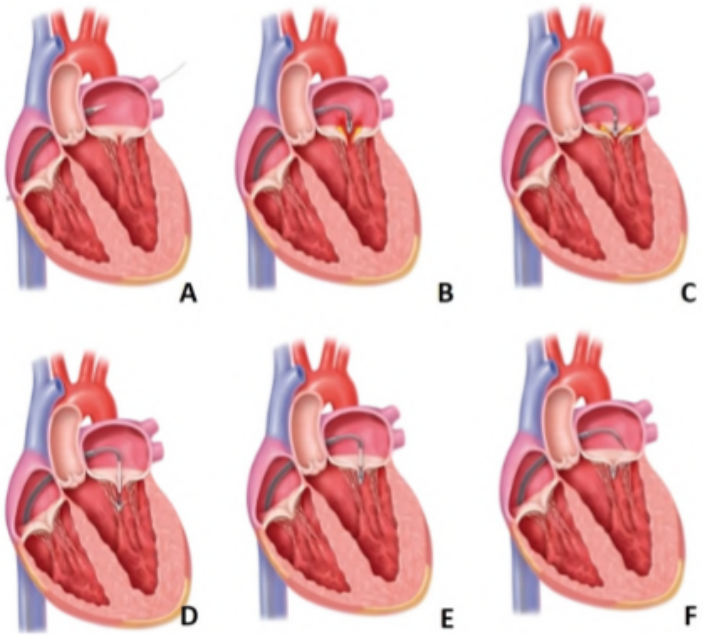

Figure 6: The 6 Steps to perform during the MitraClip surgical procedure. (A) Transseptal puncture. (B) Advancement of the Catheter Delivery System towards the Mitral Valve. (C) Positioning the MitraClip above the Mitral Valve leafltes. (D) Advancement of the Catheter Delivery System into the left ventricle. (E) Grasping of the leaflets and evaluating adequate leaflet insertion into the clip. (F) Clip release and assessment of the result. Source: Abbott [23].

clinical outcomes. However, the intrinsic repetitiveness of the task, together with the high physical workload and cognitive demand imposed on the operator, motivates the development of automatic or semi-automatic navigation systems for autonomous TMVR. Such systems have the potential to expand patient access to mitral valve repair by reducing dependence on highly specialized personnel in the operating room, while simultaneously decreasing procedural costs and maintaining clinical outcomes comparable to those of conventional manually performed MV repair procedures.

1.5. Aim of the Work

The aim of this thesis is to address the autonomous actuation and navigation of a robotic catheter system for mitral valve repair, with the goal of enabling the catheter tip to accurately follow an estimated optimal trajectory in a dynamic cardiovascular environment. Achieving this objective requires the formulation of suitable inverse kinematics (IK) models capable of relating the task space of the system, defined in terms of catheter tip position, to the corresponding actuation variables governing catheter motion.
In this context, the IK models take as input a sequence of target points describing the desired trajectory and compute the associated actuation commands required to steer the catheter toward those points. The target trajectory is time-varying as a consequence of the physiological motion of the mitral valve. To account for this behavior, an Extended Kalman Filter is employed to estimate and predict the future valve position from noisy measurements, providing a filtered and time-consistent reference for motion planning. Based on this prediction, a task-space Model Predictive Trajectory Planner framework is used to generate an optimal sequence of target positions that guides the catheter tip toward the moving valve while respecting actuation and smoothness constraints.
Within this control architecture, the mapping between the task-space trajectory using a Least Squares Online Jacobian Update and the catheter actuation space is achieved through inverse kinematics. The primary objective of this thesis is, therefore, the development, implementation, and comparative evaluation of different IK strategies for the MitraClip catheter system. Specifically, two IK models are investigated: an analytical model derived from geometric and kinematic assumptions and a data-driven model identified from experimental observations. To cope with modeling uncertainties, nonlinearities, and time-varying catheter behavior, an online Least-Squares Jacobian estimation strategy is integrated into the control loop, allowing continuous refinement of the kinematic mapping during execution.
Starting from a target input coming from Ultrasound (US) imaging , the proposed pipeline first predicts the

valve motion using the Extended Kalman Filter, then computes an optimal
Overall, the ultimate objective of this dissertation is to contribute to the development of robust and accurate autonomous navigation strategies for robotic-assisted mitral valve repair by integrating state estimation, predictive control, adaptive kinematic modeling, and experimental validation.
The remainder of this dissertation is organized as follows:

- **Chapter 1** presents an overview of mitral valve disease, the associated clinical challenges, and the current interventional treatment strategies, highlighting their benefits and limitations.
- **Chapter 2** reviews the state of the art in mitral valve motion modeling, tendon-driven continuum robot modeling, and trajectory planning techniques for moving target tracking.
- **Chapter 3** describes the proposed control architecture and research methodology, including the Extended Kalman Filter, Model Predictive Trajectory Planning framework, inverse kinematics models, and the online Jacobian estimation strategy.
- **Chapter 4** details the experimental setup and validation protocol used to assess the proposed models and control framework.
- **Chapter 5** discusses the experimental results and compares the performance of the different inverse kinematics approaches.
- **Chapter 6** concludes the dissertation and outlines possible directions for future research.

2. State of the Art

This chapter presents the state of the art in continuum robots (CRs). It first outlines the distinctive features that make CRs particularly promising for minimally invasive surgery, highlighting representative and well-established clinical applications.
Following a brief overview of CR classification, the chapter focuses on CR modeling, providing a detailed description of both analytical and data-driven approaches. The respective advantages and limitations of these methods are then critically discussed, emphasizing the need for an accurate, robust, and repeatable modeling framework for CRs.
Finally, techniques for modeling mitral valve (MV) dynamics are reviewed, concluding with an overview of moving-target tracking strategies adopted in related research fields.

2.1. Continuum Robots

Continuum robotics has experienced significant growth in recent years, attracting considerable attention from the scientific community and becoming a widely investigated research field worldwide [38]. Given its recognized potential, further substantial advancements are expected in the near future.
Continuum robotics is a subfield of robotics that aims to replicate and emulate, the remarkable dexterity and adaptability exhibited by certain biological systems—such as snakes, elephant trunks, and octopus tentacles—which are capable of navigating highly cluttered environments. Although a universally accepted definition has not yet been established, CRs are generally described as continuously bending robotic systems characterized by compliant structures and an effectively infinite number of joints and degrees of freedom (DoFs).
These features enable CRs to deform smoothly along their entire length, thereby exhibiting exceptional flexibility and adaptability [39]. As a result, CRs can navigate narrow, confined, and highly complex environments while executing a wide range of sophisticated motions. Such bio-inspired capabilities distinguish CRs from traditional rigid-link robots and, more importantly, extend robotic applicability to domains that were previously inaccessible or only marginally addressed by conventional robotic systems.
In particular, CRs have already demonstrated a significant impact in healthcare applications and are expected to further transform clinical practice in the coming years [40]. CRs are widely regarded as a key enabling technology for the next generation of medical devices and as a fundamental innovation for expanding the frontiers of minimally invasive and interventional medicine [39].

2.1.1. Continuum Robots in Medicine

As discussed in Chapter 1, minimally invasive surgery (MIS) has demonstrated significant clinical advantages and is now well established in the routine treatment of mitral regurgitation (MVR), influencing surgical techniques across multiple medical specialties [41]. An overview on medical applications of CRs is presented in Figure 7.
However, MIS techniques remain technically demanding from the surgeon's perspective due to differences in ergonomics, sensory feedback, dexterity, and procedural intuitiveness compared to conventional open surgery [42]. In this context, the integration of CRs into medical robotics has the potential to further extend the

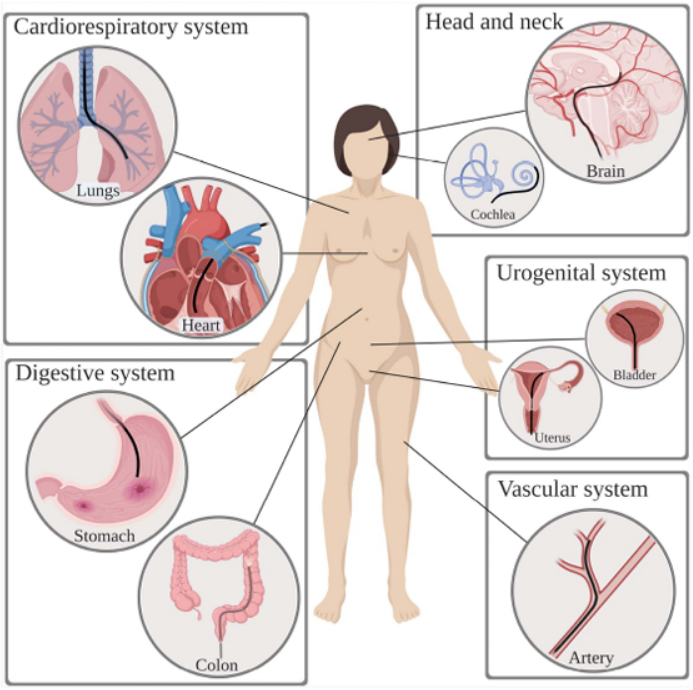

Figure 7: Applications of medical CRs for accessing hard-to-reach regions in a minimally invasive manner, including the cardiorespiratory, digestive, head and neck, urogenital, and vascular systems. Adapted from [39].

capabilities of MIS.
Owing to their compliant, continuously deformable, and miniaturized structures, CRs enable improved navigation within the patient's body, facilitate access to anatomically complex or difficult-to-reach surgical sites through nonlinear trajectories, and enhance procedural dexterity and safety. In particular, CRs can significantly improve current interventions when access to challenging anatomical regions is critical or associated with elevated risk, and they may also foster the development of novel surgical techniques.
Several CR-based systems have already reached commercial deployment [41] and are being progressively adopted in clinical practice, further supporting the promising outlook of CR technology in healthcare. Nevertheless, despite substantial progress, further advancements remain strongly dependent on addressing key challenges related to modeling, sensing, control, and fabrication—topics that are currently central within the robotics research community [41].
Before focusing on CR modeling strategies, a concise classification of CRs is presented.

2.1.2. Continuum Robots Classification

CRs can be classified according to different criteria, depending on their actuation principle, actuation location, and intended medical application [43]. Based on the actuation mechanism, continuum robots can be categorized as follows:

- **Tendon-driven catheters**: These systems consist of a central flexible backbone around which multiple antagonistic tendons are routed. Actuation is achieved by pulling the tendons, either manually or via motors, generating bending-inducing torques at the distal end. Tendon-driven catheters can be further classified into single-section or multi-section CRs, depending on the number of independently actuated segments.
- **Magnetic navigation catheters**: These catheters feature a magnetic distal tip that is steered through externally generated magnetic fields. The operator controls the tip motion by adjusting the spatial distribution of the magnetic field [44].
- **Soft material-driven catheters**: These systems are fabricated using smart or compliant materials, such as shape memory alloys or soft polymers, which enable continuous bending through intrinsic material deformation rather than external actuation mechanisms.
- **Hydraulically actuated catheters**: These robots are composed of one or more hydraulic chambers or bellows. By varying the internal hydraulic pressure, the length of each chamber changes, resulting in controlled bending of the catheter.

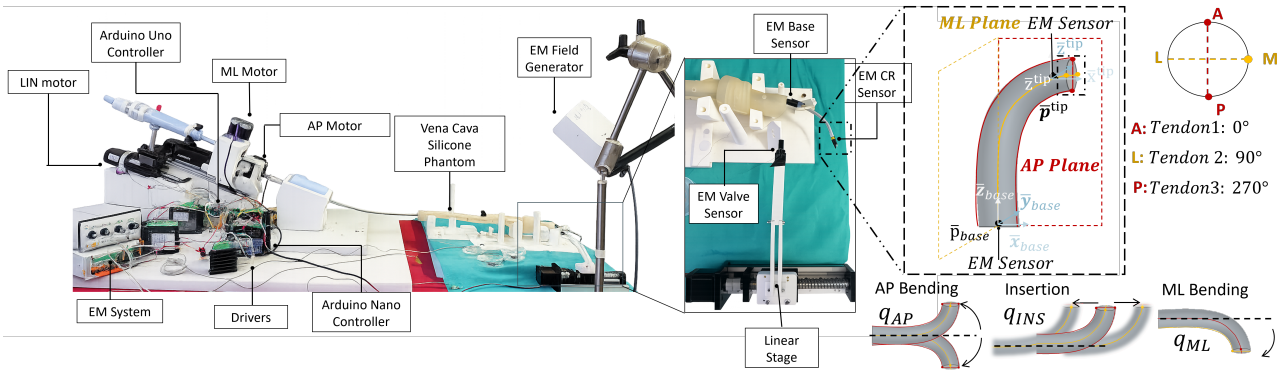

Figure 8: Left: Experimental testbed for validation of the proposed predictive control framework, including the motorized tendon-driven continuum robot (LIN, ML, AP actuation), motor drivers, and Arduino-based control units; a patient-specific vena cava silicone phantom; and an electromagnetic (EM) tracking system with three 6-DoF sensors (base, tip, and valve-mounted) providing real-time robot and target pose measurements. A motorized linear stage reproduces physiologically inspired valve motion. Right: Kinematic structure and actuation layout of the tendon-driven continuum robot, showing backbone reference frames and EM sensor placement, tendon cross-section (ML at 0°, antagonistic AP pair at 90° and 270°), and representative motions generated by the 3 Degrees of Actuation: AP bending, insertion, and ML bending.

In addition to the actuation mechanism, CRs can be classified based on the location of actuation forces:

- **Intrinsic actuation**: Actuation occurs within the deformable structure of the robot itself. Examples include magnetic, hydraulic, and soft material-driven CRs.
- **Extrinsic actuation**: Actuation forces are generated outside the robot structure and transmitted through mechanical elements, such as tendons. Tendon-driven CRs belong to this category.

Finally, CRs can also be classified according to their intended medical application. This classification depends on design parameters such as diameter, length, tip geometry, presence of lumens, surface coatings, and mechanical properties including stiffness and torque transmission capability [43].

2.2. Tendon-Driven Steerable Continuum Robots (TDSCR)

Among the CR architectures described above, tendon-driven steerable continuum robots (TDSCRs) offer a favorable trade-off between manufacturing cost, clinical effectiveness, and ease of handling in medical practice. Compared to magnetically steered systems, TDSCRs typically require simpler and less expensive manufacturing processes, while still providing adequate dexterity and controllability for a wide range of interventional procedures.

A representative example of this class of robots is the MitraClip delivery system, which can be modeled as a tendon-driven steerable CR. The relatively low manufacturing cost of such devices enables their non-reusable design, which is often preferred in clinical environments for safety and sterilization reasons.

Due to these characteristics, TDSCRs have gained widespread adoption in minimally invasive interventions. However, their flexible and compliant nature introduces significant challenges in modeling and control, arising from nonlinear kinematics, friction, backlash, and interaction with the surrounding environment. For this reason, the following chapters focus on a description of the used robotic system and different strategies for modeling and controlling TDSCRs, ranging from analytical approaches to data-driven and hybrid methods, highlighting their strengths and weaknesses

2.3. The Robotized MitraClip Device

The device used in this work is a robotized version of the MitraClip system, originally developed in [45], featuring three Degrees of Actuation. Specifically, the system is equipped with a linear motor for catheter insertion (INS), a stepper motor actuating the antagonistic A–P tendons, and an additional motor controlling the Medial (M) tendon.

This robotic platform exhibits several distinctive characteristics that significantly affect both modeling and control. These aspects are summarized below.

- **Cross-influence between medial and antero–posterior tendons and insertion**: Due to the con-

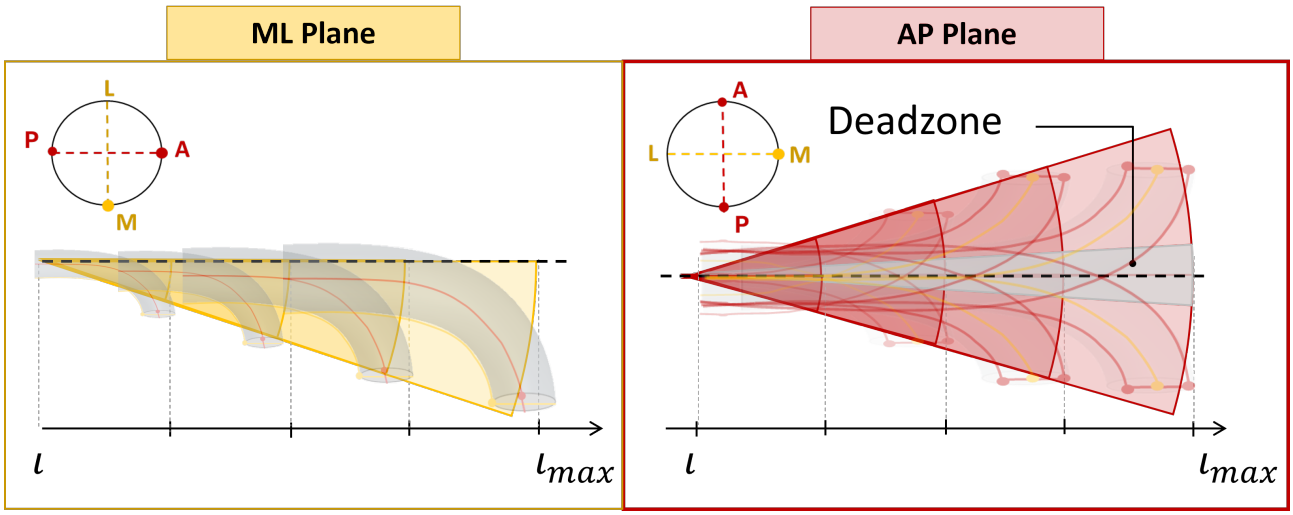

Figure 9: Workspace characterization of the tendon-driven CR in the two orthogonal bending planes. On the left: reachable workspace in the Medio–Lateral (ML) plane as a function of the insertion level ι. On the right: reachable workspace in the Antero–Posterior (AP) plane. In the AP direction, a central deadzone is observed due to the presence of the two antagonistic tendons that become simultaneously slack around the neutral configuration, resulting in a range of actuation with negligible tip motion.

tinuum nature of the catheter, the effect of M tendon actuation on the catheter tip motion strongly depends on the tension state of the AP tendons. In particular, both the magnitude of the tip displacement and the resulting direction induced by M tendon actuation vary as a function of the anterior tendon tension. Additionally, the reachable workspace while bending one tendon is heavily influenced by the insertion level ι (see Fig.9). This coupling introduces nonlinear cross-influences between actuation planes, which are difficult to capture using purely decoupled or static models.

- **Presence of dead-zones**: The catheter exhibits a dead-zone in the AP plane, corresponding to the transition region between effective A and P tendon tension (see Fig 8). Within this region, motor actuation does not result in any observable motion of the catheter tip. The number of insertion motor steps required to switch from one tendon being effectively tensioned to the other is not constant and depends on multiple factors:
  1. the degree of catheter wear, as experimentally observed by a progressive increase in the required number of actuation steps with usage;
  2. catheter-to-catheter variability, with differences of up to 30% observed between different devices.

  These characteristics render any dead-zone mapping strategy based solely on motor step counting unreliable and non-reproducible.
- **Presence of tendon hysteresis**: A hysteresis phenomenon is observed in tendon actuation. Specifically, when a tendon is repeatedly tensioned for a given number of actuation steps and is subsequently relaxed, or vice versa, the catheter tip may remain stationary for a certain period before motion is observed. The magnitude of this effect varies across different catheters, depends on the degree of mechanical wear, and is also influenced by the insertion depth of the catheter.
- **Physical actuation limits of the tendon–motor coupling**: Each tendon–motor pair is subject to physical actuation limits, beyond which additional motor commands do not result in further tendon displacement. These limits depend on the mechanical coupling between motors and tendons and cannot be directly measured due to the absence of force or tendon tension sensors. When an actuation limit is reached, further commands in the same direction must be explicitly inhibited to prevent excessive tendon tension and potential damage to the device.
- **Tendon relaxation induced by catheter insertion**: Catheter insertion introduces an additional source of nonlinearity, as it can lead to partial relaxation of the M, A, or P tendons, depending on the current configuration. While this relaxation may restore physical actuation capability in a given direction, the absence of direct tendon tension measurements prevents the control system from detecting this state change. This behavior exhibits significant catheter-to-catheter variability: some devices show relaxation in both tendons, while others do not. Moreover, the phenomenon depends on tendon wear and on the applied tendon tension itself, making it particularly challenging to characterize through an analytical model.

2.3.1. Continuum Robots Modeling

Analytical modeling approaches have been widely adopted to approximate the kinematics and dynamics of CRs, particularly in applications where a clear physical interpretation of the system behavior is required [46]. Among the most commonly used analytical models are the constant curvature (CC) formulation [47], the piecewise constant curvature (PCC) approximation [48], and more complex dynamic models based on Cosserat rod theory [49].
The CC model assumes that each deformable segment of the robot bends with a uniform curvature, effectively representing the robot shape as an arc of a circle. This assumption leads to closed-form expressions for the forward and inverse kinematics, significantly reducing computational complexity. While this simplification neglects local variations in curvature, the CC model has proven sufficiently accurate for many practical scenarios and is therefore extensively used in real-time control and planning applications [50, 51]. The PCC model extends this concept by dividing the robot into multiple segments, each characterized by its own CC. This approach improves geometric accuracy at the cost of increased model dimensionality and computational burden, while still preserving analytical tractability.
In contrast, dynamic models based on Cosserat rod theory provide a more faithful representation of CRs by explicitly modeling distributed forces, moments, and deformations along the robot backbone. These models are capable of capturing complex phenomena such as bending–torsion coupling, shear, and interaction with external loads, leading to high-fidelity predictions of robot behavior. However, the increased modeling accuracy comes at the expense of significant computational complexity. Moreover, Cosserat-based formulations strongly depend on precise knowledge of material properties, geometric parameters, and boundary conditions, which are often difficult to identify accurately in practice. As a result, their direct use in real-time surgical control scenarios is generally impractical.
To address the limitations of computational cost associated with complex analytical models, data-driven modeling approaches have gained increasing attention in recent years. By leveraging machine learning techniques, these methods aim to learn the mapping between actuation space and task space directly from experimental data, without requiring an explicit physical model. Supervised learning techniques are commonly employed in this context, including feed-forward neural networks [52–54] and regression-based approaches [55]. These models are particularly attractive due to their fast inference times once trained, making them suitable for real-time applications.
Furthermore, recurrent neural networks have been proposed to capture the temporal and dynamic characteristics of soft and continuum manipulators [56], enabling the modeling of history-dependent effects such as hysteresis and rate-dependent behavior. Despite their promising performance, data-driven approaches are inherently dependent on the quality, quantity, and representativeness of the training data. This dependency can limit their ability to generalize to unseen conditions, especially in highly variable and patient-specific anatomical environments encountered in minimally invasive surgery (MIS). Additionally, machine learning models are susceptible to issues such as overfitting and lack of interpretability, requiring extensive validation and carefully designed datasets to ensure robustness and safety.
Overall, modeling CRs inevitably involves a trade-off between model complexity, computational efficiency, and accuracy. Simplified frameworks such as rigid-link approximations and CC models typically offer low-order spatial accuracy but are computationally efficient and well suited for real-time implementation. However, they fail to account for important real-world effects, including friction, tendon slack, dead zones, gravity, and torsional deformations, whose neglect may compromise model validity [39]. Incorporating such nonlinear effects within analytical models, as in Cosserat rod theory, substantially increases model fidelity but leads to a dramatic rise in computational cost, often rendering these approaches unsuitable for practical real-time control applications.

2.3.2. Analytical Models for Continuum Robots: Constant Curvature

Within the spectrum of analytical modeling strategies for CRs, CC approaches have proven to be particularly effective when applied to tendon-driven catheters in minimally invasive cardiac procedures. In this context, Bicchi et al. [54] proposed a CC-based modeling framework for MitraClip catheter tip control, demonstrating that relatively simple kinematic representations can outperform more complex models in practical scenarios. Their results showed significantly reduced computation times while simultaneously achieving improved trajectory following and target positioning accuracy when compared to higher-order or fully dynamic models.
These findings highlight an important aspect of CR modeling: increased model complexity does not necessarily translate into better control performance. In fact, robustness, numerical stability, and real-time feasibility of a model often outweigh the benefits of higher-fidelity physical descriptions. The CC assumption, by reducing the system to a low-dimensional configuration space, enables fast inverse kinematic computations and facilitates integration with higher-level control strategies, such as trajectory planning and feedback control.
In the proposed model, the catheter is actuated by three tendons. Two antagonistic tendons enable bending in

the AP plane, while a third tendon controls bending in the ML plane. In addition, the system features one degree of actuation (DoA) for linear INS, allowing the backbone length to be increased. Overall, the actuation space consists of three DoAs: one for INS, one for ML bending, and one for AP bending obtained by simultaneously actuating the two antagonistic tendons. By appropriately pulling the tendons and adjusting the insertion depth, the catheter tip position can be accurately controlled in three-dimensional space.
To establish the relationship between the catheter tip position in task space and the tendon actuation variables, a constant curvature (CC) model is adopted. Under the CC assumption, the robot backbone is modeled as a circular arc characterized by a reduced set of geometric parameters. Specifically, the configuration space of the robot can be fully described by three quantities: the arc length $l(\mathbf{p})$, the curvature $\kappa(\mathbf{p})$, and the curvature angle $\phi(\mathbf{p})$, as shown in Fig. 4. The inverse kinematic mapping

$$\mathbf{q} = f_c(\mathbf{p})$$

thus relates the tip position in task space to the actuation variables in configuration space.
Let the catheter tip position be defined as

$$\mathbf{p}(s) = \begin{bmatrix} x(s) \\ y(s) \\ z(s) \end{bmatrix}, \mathbf{p}(s) \in \mathbb{R}^3, \tag{1}$$

where s denotes the arc-length parameter along the backbone. The curvature angle $\phi(\mathbf{p})$, describing the orientation of the bending plane, is computed as

$$\phi(\mathbf{p}) = \operatorname{atan2}(y, x). \tag{2}$$

The curvature magnitude $\kappa(\mathbf{p})$ is obtained as

$$\kappa(\mathbf{p}) = \frac{2\sqrt{(x^2 + y^2)})}{x^2 + y^2 + z^2} \tag{3}$$

while the arc length is given by

$$\ell(\mathbf{p}) = \frac{\theta}{\kappa} \tag{4}$$

where

$$\theta = \cos^{-1}\Big(1 - \kappa\sqrt{(x^2 + y^2)}\Big) \tag{5}$$

represents the angle subtended by the circular arc.
Once the geometric parameters of the configuration space are determined, the tendon length variations can be computed. The displacement of the i-th tendon is expressed as

$$\delta L_i = -\frac{d}{2}\,\theta\cos\left(\frac{i\pi}{2} - \phi\right), \tag{6}$$

where $i \in \{0, 1, 3\}$ denotes the tendon index and d is the diameter of the continuum robot. Due to the antagonistic arrangement of the AP tendons, their displacements are equal in magnitude and opposite in sign. Finally, the actuation vector $\mathbf{q} \in \mathbb{R}^3$ is defined as

$$\mathbf{q}(\mathbf{p}) = f_c(\mathbf{p}) = \begin{bmatrix} l \\ -\dfrac{d}{2}\,\theta\cos(-\phi) \\ \dfrac{d}{2}\,\theta\cos\Big(\dfrac{\pi}{2} - \phi\Big) \end{bmatrix}, \tag{7}$$

where q_1 corresponds to the linear insertion actuation, q_2 to ML bending, and q_3 to AP bending.
The proposed control strategy is formulated in the task space and is based on the position error defined as

$$\delta\mathbf{p} = \overline{\mathbf{p}} - \hat{\mathbf{p}}, \tag{8}$$

where $\overline{\mathbf{p}}$ denotes the desired catheter tip position, while $\hat{\mathbf{p}}$ represents the measured tip position.
Small variations in the task space, $\delta\mathbf{p}$, can be locally related to variations in the actuation space, $\delta\mathbf{q}$, through a first-order linear approximation:

$$\delta\mathbf{q}(\mathbf{p}) \approx \mathbf{J}_{f_c}(\mathbf{p})\,\delta\mathbf{p}, \tag{9}$$

where $\mathbf{J}_{f_c}(\mathbf{p})$ is the Jacobian of the inverse kinematic mapping $f_c(\mathbf{p})$ introduced in Eq. (7), defined as

$$\mathbf{J}_{f_c}(\mathbf{p}) = \frac{\partial \mathbf{q}}{\partial \mathbf{p}}. \tag{10}$$

By expanding the partial derivatives of the actuation variables $\mathbf{q}(\mathbf{p}) = [\, l,\ q_2,\ q_3 \,]^\top$ with respect to the task space coordinates (x, y, z), the Jacobian matrix can be expressed as

$$\mathbf{J}_{f_c}(\mathbf{p}) = \begin{bmatrix} \dfrac{\partial l}{\partial x} & \dfrac{\partial l}{\partial y} & \dfrac{\partial l}{\partial z} \\ \dfrac{\partial}{\partial x}\left(-\dfrac{d}{2}\theta\cos(-\phi)\right) & \dfrac{\partial}{\partial y}\left(-\dfrac{d}{2}\theta\cos(-\phi)\right) & \dfrac{\partial}{\partial z}\left(-\dfrac{d}{2}\theta\cos(-\phi)\right) \\ \dfrac{\partial}{\partial x}\left(\dfrac{d}{2}\theta\cos\left(\dfrac{\pi}{2}-\phi\right)\right) & \dfrac{\partial}{\partial y}\left(\dfrac{d}{2}\theta\cos\left(\dfrac{\pi}{2}-\phi\right)\right) & \dfrac{\partial}{\partial z}\left(\dfrac{d}{2}\theta\cos\left(\dfrac{\pi}{2}-\phi\right)\right) \end{bmatrix}. \tag{11}$$

The Jacobian describes how infinitesimal variations of the tip position in task space affect the corresponding actuation variables. At each control iteration, the Jacobian is evaluated online by substituting the current measured tip position $\hat{\mathbf{p}}$ into Eq. (11), yielding a numerical approximation valid in the local neighborhood of the current configuration. This Jacobian is then used to compute the required actuation variation $\delta\mathbf{q}$ according to Eq. (9).
The control effort applied to the actuators is obtained through a proportional (P) controller defined as

$$\mathbf{u} = k\,\delta\mathbf{q}, \tag{12}$$

where k is a scalar proportional gain and $\mathbf{u} \in \mathbb{R}^3$ represents the commanded variation in tendon lengths and insertion.
Since the catheter is actuated by stepper motors, the continuous control effort $\mathbf{u}$ is mapped to discrete motor commands. For the i-th actuator, the number of motor steps N_i is computed as

$$N_i = \frac{u_i}{\text{step}_i}, \tag{13}$$

where u_i is the i-th component of the control vector $\mathbf{u}$ expressed in terms of length variation, and step_i denotes the linear displacement corresponding to a single motor step.
Ideally, the tendon actuation planes are aligned with the $x-z$ and $y-z$ planes, corresponding to ML and AP bending, respectively (Fig. 4). Due to manufacturing tolerances and material compliance, this alignment is not guaranteed in the considered system. A calibration procedure was therefore performed to identify the actual actuation planes and align them with the sensor reference frame.
Two 6-DoF electromagnetic sensors were used during calibration. One sensor was placed at the base of the CR, on the tip of the sheath catheter, and one at the robot tip. The base sensor was used as reference, while the tip sensor provided pose measurements during catheter motion.
Calibration data were collected by actuating the catheter along the AP bending direction. For each sampled configuration, the vector connecting the base and tip sensor positions was computed. The set of collected vectors was processed using singular value decomposition [57] to estimate the normal vector of the plane best fitting the measured motion. The angle between this normal vector and the sensor coordinate axes was then used to compute a rotation matrix about the sensor z-axis.
The resulting transformation was applied to both base and tip measurements, aligning the AP bending plane with the sensor y-axis and the ML bending plane with the sensor x-axis. All tip poses were finally expressed in the base sensor frame. Additional details on the calibration procedure are reported in [58].

2.4. Position Control on Moving Target

Controlling a robotic system to accurately reach and track a moving target is a well-known problem in robotics, particularly relevant in applications where the target dynamics are time-varying and partially unpredictable. In these scenarios, the control objective extends beyond static point regulation and requires continuous trajectory generation and real-time adaptation to target motion.
A common formulation of this problem relies on trajectory planning and tracking approaches, where the robot motion is planned over a finite or infinite horizon while accounting for system constraints, dynamics, and target evolution. Among the most widely adopted strategies, Model Predictive Control (MPC) and Reinforcement Learning (RL) have emerged as effective tools for addressing moving target control.
Model Predictive Control approaches formulate the trajectory planning problem as a constrained optimization problem solved over a receding horizon. At each control step, the future evolution of both the robot state and

the target is predicted using a system model, and an optimal control sequence is computed by minimizing a cost function that typically penalizes tracking error, control effort, and constraint violations. Only the first control input is applied, and the optimization is repeated at the next time step using updated state measurements. MPC offers several advantages for moving target tracking, including the explicit handling of input and state constraints, robustness to disturbances through frequent replanning, and strong theoretical guarantees when an accurate model is available.

Reinforcement Learning-based approaches address moving target control by learning a control policy that directly maps system states to actions through interaction with the environment [59]. In this framework, the moving target is incorporated into the state representation, and the learning objective is defined through a reward function that promotes accurate tracking, smooth motion, and stability. RL methods can implicitly handle complex nonlinear dynamics and unmodeled effects, making them attractive for systems where analytical modeling is challenging. [60] Furthermore, once trained, RL policies can provide fast inference at runtime. Nonetheless, RL-based controllers often require large amounts of training data, careful reward shaping, and extensive validation to ensure stability and safety.

Both MPC and RL approaches can be framed within the broader class of rendezvous problems, in which the control objective is to drive the robot to intercept or track a target whose motion evolves over time. In such scenarios, the relative dynamics between the robot and the target play a central role, and successful convergence requires synchronization in both spatial position and timing. Consequently, significant effort must be devoted to accurate modeling of both the end-effector and the target dynamics.

This formulation is particularly relevant in catheter-based interventions, where the robotic tip must continuously adapt its motion to compensate for physiological disturbances, such as cardiac and respiratory-induced target displacements. Although rendezvous problems have been extensively studied in other domains—such as aerospace and defense applications [61, 62] and autonomous aerial systems [63], only limited examples exist in the context of tendon-driven robots [64, 65] and biomedical applications. To the best of our knowledge, in these latter domains MPC [66] and RL [59] approaches have thus far been investigated primarily for static target scenarios.

In line with the state-of-the-art approaches for trajectory planning and control of CRs [67], and consistently with the Constant Curvature modeling framework described in Section 2.3.2, a baseline Model Predictive Control (MPC) formulation based on the analytical inverse kinematic model is implemented. This approach represents a fully model-based solution and is used as a reference implementation for comparison with the adaptive and data-driven strategies proposed later in this work.

In this baseline formulation, the MPC directly optimizes increments in the actuation space, while the evolution of the catheter tip position is predicted using the inverse of the analytical Jacobian derived from the constant curvature model. The internal prediction model adopted by the MPC is expressed as

$$\mathbf{p}_{k+1} = \mathbf{p}_k + \mathbf{J}_{f_c}^{-1}(\mathbf{p}_k)\,\mathbf{u}_k, \tag{14}$$

where $\mathbf{p}_k \in \mathbb{R}^3$ denotes the catheter tip position at the k-th prediction step, $\mathbf{u}_k \in \mathbb{R}^3$ represents the optimized actuation increment, and $\mathbf{J}_{f_c}^{-1}(\mathbf{p}_k)$ is the inverse of the analytical Jacobian associated with the mapping $\mathbf{q} = f_c(\mathbf{p})$.

Given a prediction horizon N, the MPC computes a sequence of actuation increments $\{\mathbf{u}_k\}_{k=0}^{N-1}$ by minimizing a cost function of the form

$$J = \sum_{k=0}^{N-1} \|\mathbf{p}_{k+1} - \mathbf{p}_N\|^2_{\mathbf{W}_{\text{pos}}} + \|\mathbf{u}_k\|^2_{\mathbf{W}_{\text{act}}}, \tag{15}$$

where $\mathbf{p}_N$ denotes the desired target position, and $\mathbf{W}_{\text{pos}}$ and $\mathbf{W}_{\text{act}}$ are positive-definite weighting matrices that penalize tracking error and actuation effort, respectively.

At each MPC iteration, the Jacobian inverse $\mathbf{J}_{f_c}^{-1}(\mathbf{p}_k)$ is evaluated using the current catheter tip position, and the resulting optimal actuation increment $\mathbf{u}_0$ is applied. Owing to its reliance on an analytical constant-curvature model, this baseline approach offers low computational complexity and fast optimization, but its performance is inherently dependent on the local validity of the model and may degrade in the presence of unmodeled effects such as tendon slack, dead zones, hysteresis, and progressive actuation-plane misalignment.

2.5. Research Gap

Based on the analysis presented in the previous sections, it is possible to identify several strengths and limitations associated with the existing control strategies for position control and trajectory planning toward moving targets. With respect to RL approaches, a primary limitation lies in their generalization capability when the target dynamics differ from those encountered during training. This limitation is particularly critical in the context of mitral valve repair, where the presence of regurgitation leads to inter-patient and intra-patient variability

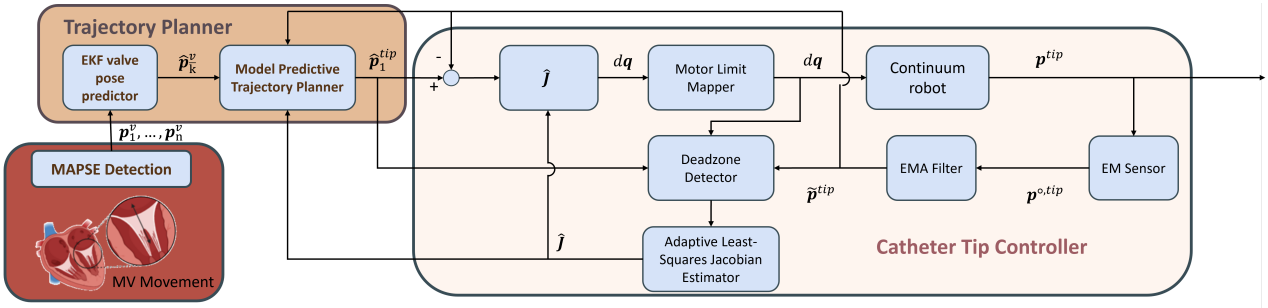

Figure 10: Proposed closed-loop control architecture integrating EKF-based MV modeling from TEE images, Model Predictive Trajectory Planning (MPTP), and Online-Estimated Jacobian (JUPD) for robust task–actuation mapping of the continuum robot.

in valve motion. Such variability further exacerbates the risk of underfitting or poor generalization of learned policies. Moreover, RL-based methods typically assume a fixed system structure during deployment. In the case of the MitraClip catheter, this assumption is violated by manufacturing tolerances that result in significant catheter-to-catheter variability. In particular, the alignment between the ML and antero-posterior AP actuation planes and their ideal orthogonal configuration may vary substantially across devices.
Additional sources of variability arise from the catheter mechanics themselves. The size of the dead zone in the AP plane, caused by the antagonistic anterior and posterior tendons, is not constant across catheters. Furthermore, repeated usage leads to progressive tendon wear, inducing changes in hysteresis behavior and effective workspace over time. Accounting for all these factors within an RL framework would require collecting an extensive and diverse dataset spanning different catheters, wear conditions, target dynamics, and sensor configurations, rendering such an approach impractical in a clinical setting.
On the other hand, MPC approaches have demonstrated the feasibility of position control for CRs in static target scenarios [66, 68]. However, their extension to dynamic target tracking in biomedical applications remains largely unexplored. In non-medical contexts, dynamic target tracking for continuum robots has been investigated using analytical models [65], yielding satisfactory but not fully conclusive results in terms of accuracy. Moreover, MPC performance is strongly dependent on model fidelity and computational efficiency, which can limit its applicability in highly nonlinear systems or in scenarios requiring fast control updates.
A common limitation shared by both RL- and MPC-based approaches is the absence of an adaptive model update during task execution. In particular, existing methods do not explicitly exploit the data collected online during control to refine the model and capture unmodeled nonlinearities. Incorporating an online model adaptation mechanism offers two key advantages: first, it improves control accuracy by continuously refining the mapping between desired task-space motion and actuation commands; second, it enhances the efficiency and effectiveness of predictive trajectory planning by providing a progressively more accurate model to the planner. Motivated by these observations, the next chapter (Section 3) introduces a control framework capable of handling dynamic targets through explicit target modeling, trajectory planning via Model Predictive Trajectory Planning (MPTP), and an adaptive data-driven control model. The proposed approach further incorporates dedicated strategies to manage catheter-specific nonlinearities, including dead zones and hysteresis, thereby addressing the limitations identified in the current state of the art.

3. Materials and Methods

This section describes the proposed navigation and control framework for catheter-based mitral valve intervention. The method relies on a task-space MPTP strategy, which computes a sequence of target positions based on a desired reference provided by an Extended Kalman Filter (EKF). The EKF processes the measured mitral valve position to estimate a filtered target trajectory, which is then supplied to the MPTP.
The overall control architecture is summarized in Algorithm 1 and graphically illustrated in the corresponding block diagram in Fig.10. To ensure notational consistency throughout this section, the main symbols and variables used in the formulation are summarized in Table 1.

3.1. Extended Kalman Filter

The oscillation direction of the MV plane can be reasonably assumed to remain constant over time [69]. Under this assumption, the dominant direction of motion is identified through a Singular Value Decomposition (SVD) applied to a set of sampled valve position measurements. Specifically, a finite window of valve pose data is

Table 1: Notation and Terminology

Symbol	Description
$\mathbf{x}$	Real (ground-truth) vector quantity or unknown vector, when specified
$\mathbf{x}^{\circ}$	Measured vector quantity
$\overline{\mathbf{x}}$	Target or reference vector quantity
$\tilde{\mathbf{x}}$	Filtered vector quantity
$\hat{\mathbf{x}}$	Estimated or optimized vector quantity
$\mathbf{x}_k$	Quantity at step k in discrete time
$\mathbf{p}^v$	Valve base position vector
$\mathbf{p}^{\text{tip}}$	Catheter tip position vector
$d\mathbf{p}$	Difference between target and actual catheter tip position vector
$d\mathbf{q}$	Actuation vector

Algorithm 1 Overall Control Algorithm

while $\|\tilde{\mathbf{p}}_k^{\text{tip}} - \tilde{\mathbf{p}}_k^v\|_2^2 > \varepsilon_{\text{track}}$ **do**
  Predict filtered valve base position $\hat{\mathbf{p}}_{k+1}^v$ using the EKF predictor (Section 3.1)
  Compute target reference position $\overline{\mathbf{p}}_{k+1}^{\text{tip}}$ via MPTP (Section 3.2)
  Compute desired actuation vector $d\mathbf{q}_k$
  Decompose $d\mathbf{q}_k$ into n incremental actuation steps $\{d\mathbf{q}_{k,i}\}_{i=1}^n$
  for $i = 1$ to n **do**
    Apply actuation increment $d\mathbf{q}_{k,i}$
  end for
  Update Jacobian estimate $\hat{\mathbf{J}}_k$ using the LS procedure (Section 3.3)
end while

collected and processed, and the principal eigenvector of the resulting data covariance matrix is selected as the unit vector describing the main oscillatory direction of the MV plane $\mathbf{d}^v$. The valve base position $\mathbf{p}_{\text{b}}^v$ is then estimated by detecting local minima of the projected signal and computing the mean of the corresponding three-dimensional points. This procedure provides a robust estimate of the reference position around which the valve oscillates, reducing sensitivity to noise and outliers (Fig.11).

An Extended Kalman Filter (EKF) is then employed to identify and predict the valve motion model, due to its online adaptability and its capability to provide state estimates at future time instants. While EKF-based prediction allows the controller to anticipate valve motion, it is worth noting that the associated prediction uncertainty increases as the prediction horizon extends beyond the current time.

At first order, the MV dynamics is approximated by a periodic motion along the identified oscillation direction, which was modeled as a double half-sine waveform. This representation is characterized by three parameters: an oscillation amplitude, a base position with an offset, and a fundamental frequency f.

Since the frequency f is the only reliable physiological measurement available, obtained from a heart-rate monitor, it is assumed to be known and is therefore used as an external input to the model. Based on this formulation, the state vector to be estimated is defined as follows. The variable p^v denotes the MV annular plane position (i.e. a scalar component) along the previously identified motion direction, which serves as the target position input to the MPTP. The variable b represents the offset of the valve plane with respect to the estimated valve base position. Finally, the variable A denotes the amplitude of the mitral annular plane systolic excursion (MAPSE). The state of the system is described by the vector

$$\mathbf{x}_k = \begin{bmatrix} p_k^v & b_k & A_k \end{bmatrix}^\top, \tag{16}$$

where $\mathbf{x}_k \in \mathbb{R}^3$ denotes the state vector at discrete time step k. The state components correspond to the valve base position $p_k^v \in \mathbb{R}$, an offset term $b_k \in \mathbb{R}$, and the amplitude $A_k \in \mathbb{R}$ of the periodic valve motion.

Let the signal period be defined as $T = 1/f$, where f denotes the motion frequency. The nonlinear state transition model captures the periodic behavior of the valve base position and is given by

$$\hat{p}_{k+1}^v = \begin{cases} A_k \sin(2\pi f t_k) + b_k, & t_k < \frac{T}{2}, \\ -A_k \sin(2\pi f t_k) + b_k, & t_k \geq \frac{T}{2}, \end{cases} \tag{17}$$

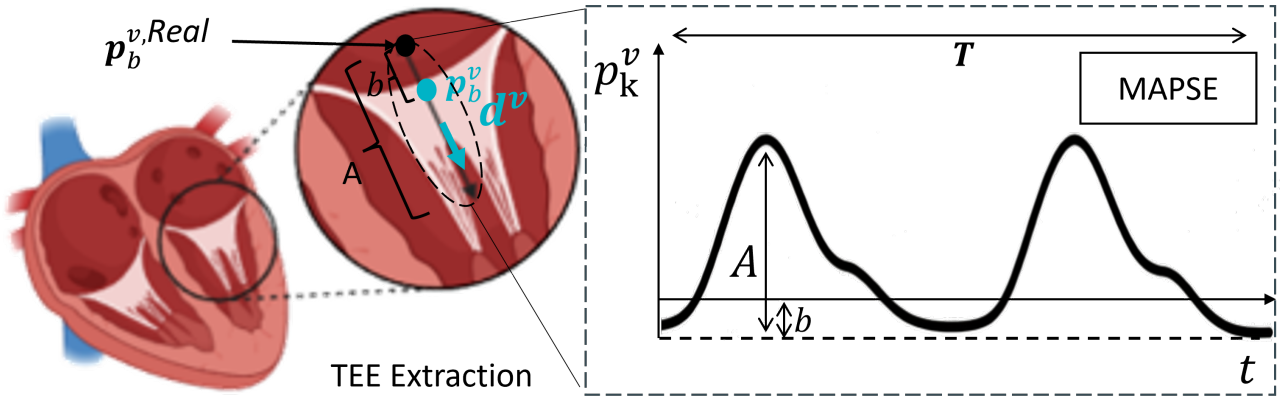

Figure 11: MAPSE identification. MV motion is described by the displacement vector $\mathbf{d}^v$ and basal point $\mathbf{p}_\mathrm{b}^v$ (cyan). A is the motion amplitude along the MV direction and b is the axial offset between $\mathbf{p}_\mathrm{b}^v$ and $\mathbf{p}_\mathrm{b}^{v,\mathrm{real}}$.

where $\hat{p}_{k+1}^v$ represents the a-priori prediction of the valve base position at step $k+1$. The remaining state components are modeled as constant, namely

$$\hat{b}_{k+1} = b_k, \tag{18}$$

$$\hat{A}_{k+1} = A_k, \tag{19}$$

reflecting the assumption that both the offset and amplitude vary slowly with respect to the sampling interval. The Jacobian matrix of the nonlinear state transition function with respect to the state vector, $\mathbf{F}_k = \partial f / \partial \mathbf{x}$, is given by

$$\mathbf{F}_k = \begin{bmatrix} 0 & 1 & \alpha(t_k) \\ 0 & 1 & 0 \\ 0 & 0 & 1 \end{bmatrix}, \tag{20}$$

where $\mathbf{F}_k \in \mathbb{R}^{3\times 3}$ and the term $\alpha(t_k)$ denotes the partial derivative of the predicted valve position with respect to the amplitude parameter A_k, defined as

$$\alpha(t_k) = \begin{cases} \sin(2\pi f t_k), & t_k < \frac{T}{2}, \\ -\sin(2\pi f t_k), & t_k \geq \frac{T}{2}. \end{cases} \tag{21}$$

The predicted state error covariance matrix is computed according to

$$\hat{\mathbf{P}}_{k+1} = \mathbf{F}_k \mathbf{P}_k \mathbf{F}_k^\top + \mathbf{Q}, \tag{22}$$

where $\mathbf{P}_k \in \mathbb{R}^{3\times 3}$ denotes the a-posteriori state covariance at step k, and $\mathbf{Q} \in \mathbb{R}^{3\times 3}$ represents the process noise covariance matrix.
The measurement model assumes that only the valve base position is directly observed. The scalar measurement equation is therefore expressed as

$$z_k = p_k^v + n_k, \tag{23}$$

where $z_k \in \mathbb{R}$ is the measured valve position and n_k is additive measurement noise. The noise term is modeled as zero-mean white Gaussian noise with variance R, i.e.,

$$n_k \sim \mathcal{N}(0, R). \tag{24}$$

Accordingly, the measurement matrix is defined as

$$\mathbf{H} = \begin{bmatrix} 1 & 0 & 0 \end{bmatrix}, \tag{25}$$

with $\mathbf{H} \in \mathbb{R}^{1\times 3}$.
The innovation sequence and its covariance are computed as

$$\mathbf{y}_k = z_k - \mathbf{H}\hat{\mathbf{x}}_k, \tag{26}$$

$$\mathbf{S}_k = \mathbf{H}\hat{\mathbf{P}}_k\mathbf{H}^\top + R, \tag{27}$$

where $\mathbf{y}_k \in \mathbb{R}$ represents the innovation and $\mathbf{S}_k \in \mathbb{R}$ its associated covariance.
The Kalman gain is then obtained as

$$\mathbf{K}_k = \hat{\mathbf{P}}_k\mathbf{H}^\top\mathbf{S}_k^{-1}, \tag{28}$$

with $\mathbf{K}_k \in \mathbb{R}^{3\times1}$. Finally, the a-posteriori state estimate and covariance update equations are given by

$$\tilde{\mathbf{x}}_k = \hat{\mathbf{x}}_k + \mathbf{K}_k\mathbf{y}_k, \tag{29}$$

$$\mathbf{P}_k = (\mathbf{I} - \mathbf{K}_k\mathbf{H})\hat{\mathbf{P}}_k, \tag{30}$$

where $\mathbf{I} \in \mathbb{R}^{3\times3}$ denotes the identity matrix. All matrices and vectors are dimensionally consistent, with a three-dimensional state vector, scalar measurements, and corresponding covariance matrices of size 3×3.
It is important to note that the Extended Kalman Filter (EKF) described above operates in a loop that is independent of the main control algorithm. During the execution of the control loop, each newly acquired measurement of the MV plane, $\mathbf{p}^{v\circ}$, triggers both the prediction and update steps of the EKF, thereby continuously maintaining the consistency of the model identification.
In contrast, when a future valve position is required solely for trajectory planning purposes, only the EKF state prediction step is executed, while the measurement update and the covariance matrix update are omitted. This choice is motivated by the fact that no new measurements are available at future time instants and that the predicted state is used exclusively to anticipate the valve motion for planning.
In this case, the elapsed time Δt between the last MPTP solution and the current time instant is first computed. Based on the previously identified valve motion parameters—namely the valve base position, the principal motion direction, and the oscillation frequency and amplitude estimated by the EKF—the future valve plane position is predicted along the identified oscillation direction.
Specifically, the scalar displacement predicted by the EKF state transition model (Eq. 17) is projected onto the valve motion direction and added to the estimated valve base position, yielding

$$\overline{\mathbf{p}}^v_{k+1} = \mathbf{p}^v_{\text{base}} + \hat{p}^v_{k+1}\,\mathbf{d}^v, \tag{31}$$

where $\mathbf{p}^v_{\text{b}}$ denotes the estimated valve base position, $\mathbf{d}^v$ is the unit vector describing the valve oscillation direction identified via SVD, and $\hat{p}^v_{k+1}$ is the scalar displacement predicted by the EKF without covariance update.
The resulting predicted valve plane position is then used as the reference target for trajectory planning and is therefore denoted as $\overline{\mathbf{p}}^v_{k+1}$ in the MPTP formulation described in the following section.

3.2. Model Predictive Trajectory Planning

To robustly handle a moving target subject to multiple sources of uncertainty and to avoid both the explicit inversion of the Jacobian matrix $\mathbf{J}$ and excessive reliance on the state transition model presented in Section 2.3.2, a task-space MPTP is proposed.
Indeed, starting from a non-optimal estimate of the state transition matrix $\hat{\mathbf{J}}$, using the same model for both the cost function formulation and position prediction may lead to suboptimal convergence behavior and increased target-reaching time. To mitigate these limitations, the proposed MPTP formulation directly optimizes the unknown predicted task-space tip positions $\mathbf{p}^{\text{tip}}_0, \ldots, \mathbf{p}^{\text{tip}}_K$, hereafter referred to as $\mathbf{x}_0, \ldots, \mathbf{x}_{K+1}$ for simplicity, over a finite prediction horizon K, according to the following rationale:
The proposed cost function $\theta(\mathbf{x}_0, \mathbf{x}_1, \ldots, \mathbf{x}_K)$ could be divided into 4 components summarized in the equation

$$\theta(\mathbf{x}_0, ..., \mathbf{x}_\text{k}, ..., \mathbf{x}_\text{K}) = \sum_{k=1}^{K}[\lambda_t(\mathbf{x}_k) + \lambda_s(\mathbf{x}_k, \mathbf{x}_{k-1}) + \lambda_a(\mathbf{x}_k, \mathbf{x}_{k-1})] + \lambda_e(\mathbf{x}_K) \tag{32}$$

with λ_t being the task cost that mimics the control effort to perform a set of control actions in the task space with respect to the target to be reached, λ_s being the smoothness cost used to reduce the likelihood of generating a solution that has an inconsistent trajectory (i.e., points scattered across the workspace in a non-smooth trajectory), λ_a being the actuation cost modeling the control effort that penalizes a set of actuation leading to points far from the optimal trajectory, and λ_e being the terminal cost acting as a "soft-constraint" to ensure the final point of the generated trajectory is as close as possible (taking into account other costs) to the final target point. The full definition of all the costs can be found in the equations below:

$$\lambda_t(\mathbf{x}_k) = (\mathbf{x}_k - \overline{\mathbf{p}}^v_{k+1})^T\mathbf{T}(\mathbf{x}_k - \overline{\mathbf{p}}^v_{k+1}), \qquad \mathbf{T} \in \mathbb{R}^{3\times3} \tag{33}$$

Table 2: Insertion-Adaptive Weighting Parameters

Symbol	Description
ι	Insertion level
$\iota_{\max}$	Maximum admissible insertion
ι_c	Insertion cutoff threshold
γ	Sigmoid steepness factor
$\alpha(\iota)$	Insertion-adaptive scheduling factor
w^-_{INS}, w^+_{INS}	Insertion weights (early / late)
$w^-_{\mathrm{ML}}, w^+_{\mathrm{ML}}$	Medio-lateral weights (early / late)
$w^-_{\mathrm{AP}}, w^+_{\mathrm{AP}}$	Antero-posterior weights (early / late)
$\mathbf{A}$	Adaptive actuation weighting matrix

$$\lambda_s(\mathbf{x}_k, \mathbf{x}_{k-1}) = (\mathbf{x}_k - \mathbf{x}_{k-1})^T \mathbf{S} (\mathbf{x}_k - \mathbf{x}_{k-1}), \qquad \mathbf{S} \in \mathbb{R}^{3\times 3} \tag{34}$$

$$\lambda_a(\mathbf{x}_k, \mathbf{x}_{k-1}) = \big(\hat{\mathbf{J}}(\mathbf{x}_k - \mathbf{x}_{k-1})\big)^T \mathbf{A} \big(\hat{\mathbf{J}}(\mathbf{x}_k - \mathbf{x}_{k-1})\big), \qquad \mathbf{A} \in \mathbb{R}^{3\times 3} \tag{35}$$

$$\lambda_e(\mathbf{x}_K) = (\mathbf{x}_K - \overline{\mathbf{p}}^v_{k+1})^T \mathbf{W} (\mathbf{x}_K - \overline{\mathbf{p}}^v_{k+1}), \qquad \mathbf{W} \in \mathbb{R}^{3\times 3} \tag{36}$$

The weighting matrices $\mathbf{T}$, $\mathbf{S}$, and $\mathbf{W}$ are empirically tuned design parameters. The matrix $\mathbf{A}$ is defined as a diagonal, insertion-adaptive weighting matrix, whose entries are updated online to progressively increase the cost associated with insertion-related actuation.

The adaptation mechanism is governed by a sigmoid-like scheduling function that modulates the relative importance of insertion with respect to medio-lateral (ML) and antero-posterior (AP) actuation components as a function of the insertion level (Fig.12. Let ι denote the insertion level, $\iota_{\max}$ the maximum admissible insertion, and ι_c a cutoff threshold defining the transition between early- and late-insertion regimes. The scheduling factor $\alpha(\iota) \in [0, 1]$ is defined as

$$\alpha(\iota) = \frac{1}{1 + \exp\!\Big(-\gamma \left(\frac{\iota}{\iota_{\max}} - \frac{\iota_{\max} - \iota_c}{\iota_{\max}}\right)\Big)}, \tag{37}$$

where $\gamma > 0$ is a steepness parameter controlling the sharpness of the transition.

Using $\alpha(\iota)$, the adaptive actuation weighting matrix is defined as

$$\mathbf{A}(\iota) = \mathrm{diag} \begin{bmatrix} (1-\alpha)\, w^-_{INS} + \alpha\, w^+_{INS} \\ (1-\alpha)\, w^-_{\mathrm{ML}} + \alpha\, w^+_{\mathrm{ML}} \\ (1-\alpha)\, w^-_{\mathrm{AP}} + \alpha\, w^+_{\mathrm{AP}} \end{bmatrix}, \tag{38}$$

where w^-_{INS}, w^+_{INS}, $w^-_{\mathrm{ML}}, w^+_{\mathrm{ML}}$, and $w^-_{\mathrm{AP}}, w^+_{\mathrm{AP}}$ denote the early- and late-insertion weights associated with insertion, medio-lateral, and antero-posterior actuation, respectively.

The behavior of the scheduling function $\alpha(\iota)$, together with the location of the cutoff ι_c, is illustrated in Fig. 12, highlighting the transition between early- and late-insertion regimes.

It is worth noting that the $actuation_{\mathrm{cost}}$ term acts solely as a soft constraint, shaping the cost function to favor insertion during the early stages of motion without suppressing medio-lateral (ML) and antero-posterior (AP) actuation. This design choice, in fact, allows for pure ML and AP movements when the target is initially located close to the catheter tip.

Finally, the full equation becomes:

$$\begin{aligned} \theta(\mathbf{x}_0, \ldots, \mathbf{x}_K) = \sum_{k=1}^{K} \Big(& (\mathbf{x}_k - \mathbf{x}_{\mathrm{target}})^T \mathbf{T} (\mathbf{x}_k - \mathbf{x}_{\mathrm{target}}) \\ & + (\mathbf{x}_k - \mathbf{x}_{k-1})^T \mathbf{S} (\mathbf{x}_k - \mathbf{x}_{k-1}) \\ & + \big(\hat{\mathbf{J}}(\mathbf{x}_k - \mathbf{x}_{k-1})\big)^T \mathbf{A} \big(\hat{\mathbf{J}}(\mathbf{x}_k - \mathbf{x}_{k-1})\big) \Big) \\ & + (\mathbf{x}_K - \mathbf{x}_{\mathrm{target}})^T \mathbf{W} (\mathbf{x}_K - \mathbf{x}_{\mathrm{target}}) \end{aligned} \tag{39}$$

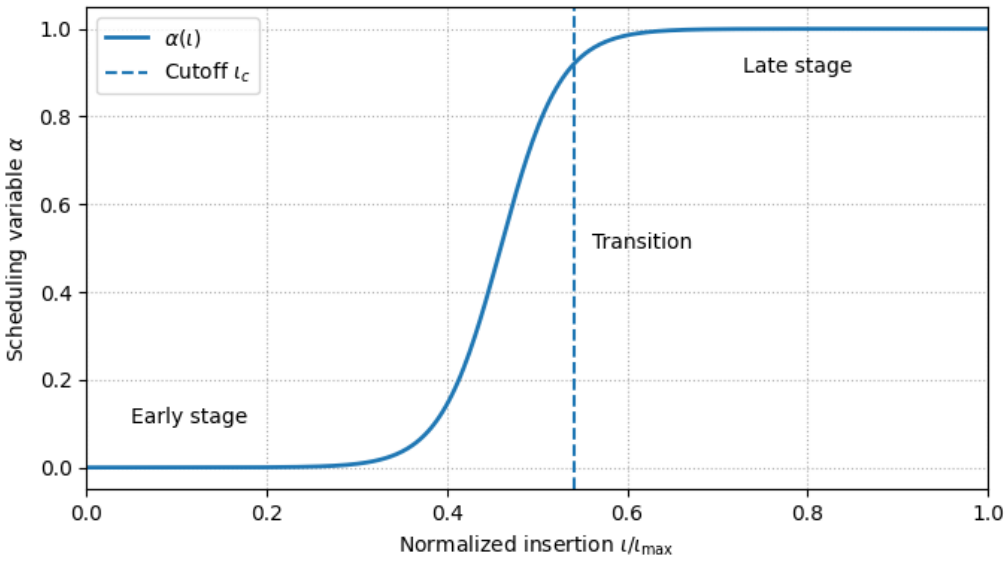

Figure 12: Insertion-adaptive sigmoid scheduling function $\alpha(\iota)$, showing the cutoff threshold ι_c and the transition between early- and late-insertion regimes.

3.3. Least Squares Data-Driven Catheter Modeling

To control the tendon-driven catheter and capture punctual non-linear dynamics, we adopt an adaptive Least-Squares model identification similar to [70]. Given the state equations defined in 2.3.2:
the desired tip position update is

$$\mathbf{p}_{k+1}^{\text{tip}} = \mathbf{p}_k^{\text{tip}} + \delta\mathbf{p}_k, \tag{40}$$

where $\overline{\mathbf{p}}_{k+1}^{\text{tip}}$ is the desired tip position, $\mathbf{p}_k^{\text{tip}}$ the actual tip position, and $\delta\overline{\mathbf{p}}_k^{\text{tip}}$ represents the target position variation of the in the task space neighborhood to reach $\overline{\mathbf{p}}_{k+1}^{\text{tip}}$.
The measured tip position after the actuation is

$$\mathbf{p}_{k+1}^{\circ} = \mathbf{p}_k^{\text{tip}} + \delta\mathbf{p}_k^{\circ}, \tag{41}$$

$$\delta\mathbf{p}_k^{\circ} = \delta\mathbf{p}_k + \boldsymbol{\varepsilon}_{\text{meas}}, \tag{42}$$

$$\boldsymbol{\varepsilon}_{\text{meas}} \sim \text{WN}\big(\mathbf{0}, \boldsymbol{\sigma}_{\text{meas}}^2\mathbf{I}\big)\,. \tag{43}$$

where $\boldsymbol{\varepsilon}_{\text{meas}} \in \mathbb{R}^{3\times1}$ is the measurement noise vector, and $\boldsymbol{\sigma}_{\text{meas}}^2 \in \mathbb{R}^{3\times1}$ contains the variance of each x, y, z measurement axis. Starting from the incremental kinematic relationship introduced above, the control action relies on the local linear approximation between task space and actuation space, expressed through the Jacobian matrix. Assuming that, in a neighborhood of the current configuration, the catheter dynamics can be locally approximated as

$$\delta\mathbf{q}_k \approx \mathbf{J}\,\delta\overline{\mathbf{p}}_k, \tag{44}$$

The problem of Jacobian adaptation can be formulated as a prediction error minimization task. In particular, given the current estimate $\hat{\mathbf{J}}_k$, the predicted actuation increment associated with a desired task-space variation is

$$\delta\mathbf{q}_k = \hat{\mathbf{J}}_k\,\delta\overline{\mathbf{p}}_k. \tag{45}$$

After applying the actuation, the measured Cartesian displacement at the next time step is $\delta\mathbf{p}_{k+1}^{\circ}$, from which the effective actuation– displacement relation can be evaluated. The corresponding estimation error is therefore defined as

$$\mathbf{e}_k = \delta\mathbf{q}_k - \hat{\mathbf{J}}_k\,\delta\mathbf{p}_k^{\circ}. \tag{46}$$

In the presence of modeling inaccuracies, measurement noise, tendon hysteresis, and configuration-dependent nonlinearities, this error is generally non-zero. Therefore, the Jacobian update can be interpreted as the search

for a correction $\delta\mathbf{J}$ that minimizes the discrepancy between predicted and measured actuation increments over a finite set of observations.
By stacking H observations, the adaptive identification problem naturally leads to a weighted Least-Squares formulation, where the objective is to minimize the squared ℓ_2 norm of the prediction errors, while accounting for measurement uncertainty and enforcing bounded variations of the Jacobian estimate. This reasoning directly motivates the cost function introduced in Eq. (47).
Given a set of H observations h, with $h \in \mathbb{N}$, we can define the cost function $C(\delta\mathbf{J})$ as the sum of the error norms squared plus an error term mimicking measurement uncertainties. However, due to the non-linearities of the problem, a forgetting factor to weight more the latest observations was implemented:

$$C(\delta\mathbf{J}) = \sum_{h=0}^{H} \rho_h \left\| \delta\mathbf{q}_{k-h} - \left(\hat{\mathbf{J}}_k + \delta\mathbf{J}\right)\delta\mathbf{p}^{\circ}_{h-k} \right\|_2^2 + \|\delta\mathbf{J}\|_F \,, \tag{47}$$

where ρ_h is defined as

$$\rho_h = \lambda_{\text{forget}}^{h} \frac{\sigma_{\text{forget}}^2}{\sigma_{\text{forget}}^2 + \|e_{k-h}\|_2^2} \tag{48}$$

where t indicates the h^{th} observation and e_{k-h} is computed as:

$$\mathbf{e}_{k-h} = d\mathbf{q}_h - \hat{\mathbf{J}}_k \left(d\overline{\mathbf{p}}_h + d(d\overline{\mathbf{p}}_h)\right) \tag{49}$$

and $d(d\overline{\mathbf{p}}_h)) = \boldsymbol{\Sigma}\, d\overline{\mathbf{p}}_h$, with $\boldsymbol{\Sigma} = \text{diag}(\sigma_x^2, \sigma_y^2, \sigma_z^2)$ to express position measurement errors due to uncertainties in the measurement system. Finally, $\|\delta\mathbf{J}\|_F$ represents the Frobenius norm of the Jacobian update, i.e.,

$$\|\delta\mathbf{J}\|_F = \sqrt{\sum_{i=1}^{m}\sum_{j=1}^{n}(\delta J_{ij})^2}, \tag{50}$$

which acts as a convex regularization term that penalizes large variations of the estimated Jacobian, thus ensuring numerical stability and preventing abrupt updates.
An important consideration concerns the preservation of the local linearity assumption underlying the Jacobian update algorithm presented above. In practice, large control inputs—particularly during the initial iterations of the control loop—may violate this assumption, producing relatively large variations in both the input and output. This can introduce instability in the Jacobian estimation and reduce the number of informative samples available, which in turn limits the accuracy of the estimated Jacobian.
To mitigate these issues, the actuation vector $\mathbf{q} = [\text{INS, ML, AP}]^T$ is divided into n smaller actuation vectors by scaling each component with respect to the maximum admissible actuation per step. These smaller vectors are applied sequentially to the motors, generating n corresponding input–output pairs ($d\mathbf{q}$, $d\overline{\mathbf{p}}$). Each pair then serves as an individual observation for the Jacobian update algorithm, allowing the method to maintain linearity assumptions locally while improving the robustness and accuracy of the estimation.
To sum up, the full Jacobian update algorithm at each new observation is illustrated below 2

3.4. Jacobian Initialization, dead-zone detection, Motor Limit Mapping

To ensure proper convergence of the Jacobian estimation algorithm presented in Section 3.3, to avoid zero-valued elements and to guarantee bounded stability of the intra-update solution, a one-time offline initialization of the Jacobian matrix was required.
Considering INS, AP and ML as the three available actuation degrees of freedom, an initialization procedure was performed by applying a set of single-axis actuation commands and measuring the corresponding end-effector displacements in Cartesian space. In particular, for each of the six possible actuation directions, 15 actuation–motion pairs were collected, resulting in a total of 90 samples.
Each sample consists of an actuation increment vector d$\mathbf{q}$ and the corresponding measured Cartesian displacement d$\overline{\mathbf{p}}$. Once the dataset was acquired, the initial Jacobian matrix was obtained via a least-squares fitting procedure, assuming a locally linear relationship between actuation space and Cartesian space:

$$\mathrm{d}\overline{\mathbf{p}} = \mathbf{J}_0\, \mathrm{d}\mathbf{q}. \tag{51}$$

The initial Jacobian estimate was then obtained by solving the Weighted Least-Squares problem in (47), enforcing $\rho_h = 1$ for all samples, thus removing temporal weighting after having collected 90 samples.
Furthermore, to prevent the inclusion of actuation–motion pairs in which no effective displacement occurred (i.e., samples collected within a workspace dead-zone), which would result in incorrect data and potentially cause

Algorithm 2 Adaptive Least-Squares Jacobian Identification

Decompose each actuation vector $d\mathbf{q} = [\text{INS, ML, AP}]^T$ into n smaller sub-actuations $d\mathbf{q}_i$, $i = 0, \ldots, n-1$
Apply all sub-actuations sequentially to the motors
Measure the resulting tip displacements $d\mathbf{p}^{\circ}_{h=i}$ for each sub-actuation
Store all pairs $\left(d\mathbf{q}_{h=i}, d\mathbf{p}^{\circ}_{h=i}\right)$ as observations
Discard the $(H+1^{th}, ..., H+n^{th})$ observation $[(d\mathbf{p}^{\circ}_{H+1}, d\mathbf{q}_{H+1}), ..., (d\mathbf{p}^{\circ}_{H+N}, d\mathbf{q}_{H+N})]$
while $\|\delta\mathbf{J}\|_F > \epsilon$ or $N_{\text{iter}} < 1000$ **do**
  Initialize $C(\delta\mathbf{J}) = 0$
  for $h = 0$ to N **do**
    Compute error $\mathbf{e}_{k-h} = d\mathbf{q}_h - \hat{\mathbf{J}}_k \left(d\overline{\mathbf{p}}_h + d(d\overline{\mathbf{p}}_h)\right)$
    Compute forgetting factor $\rho_h$using (48)
    Update Cost Function $C(\delta\mathbf{J}) = C(\delta\mathbf{J}) + \rho_h \left\| \delta\mathbf{q}_{k-h} - \left(\hat{\mathbf{J}}_k + \delta\mathbf{J}\right)\delta\mathbf{p}^{\circ}_{h-k} \right\|_2^2$
  end for
  Add $\|\delta\mathbf{J}\|_F$ to $C(\delta\mathbf{J})$
  Solve for $\delta\mathbf{J}$
  Compute $\hat{\mathbf{J}} = \hat{\mathbf{J}} + \delta\mathbf{J}$
end while

divergence of the Jacobian optimization process, a dedicated dead-zone detection algorithm was implemented, consisting of:

- **Exponential Moving Average (EMA) filter**: an Exponential Moving Average (EMA) filter is characterized by the following recursive equation:

$$y(t) = \alpha\, x(t) + (1-\alpha)\, y(t-1), \tag{52}$$

  with $y(t)$ being the filtered quantity at time instant t, $y(t-1)$ being the filtered quantity at the previous time instant and $x(t)$ being the measured quantity, where α controls the trade-off between noise attenuation and responsiveness of the filter, with larger values giving more weight to recent samples. The 3 position components coming from the EM sensor of the catheter tip and base were filtered using $\alpha = 0.1$ and initialized simply with $y(0) = x(0)$
- **Thresholding the difference between points**: After performing an actuation, the EMA-filtered starting position is compared with the position measured after the actuation by computing the Euclidean distance between the two points. If this distance is below a predefined threshold, the resulting $d\overline{\mathbf{p}}$ is discarded and not used in the Jacobian estimation process described in Section 3.3.
  Furthermore, a special treatment is required for the AP tendon. As discussed in Section 2.3, the MitraClip G4 exhibits both a consistent dead-zone in the middle of the actuation workspace and an interdependence between insertion and the degree of AP tendon relaxation. To avoid sampling within a dead-zone or during sudden AP relaxation, which would lead to incorrect Jacobian estimates—once a pure AP actuation is performed, the Euclidean distance is evaluated. Instead of simply discarding movements below the threshold, subsequent actuations are temporarily blocked, and another pure AP actuation is executed. If the distance remains below the threshold, the system identifies a dead-zone and repeats the same actuation until a movement above the threshold is detected. Afterward, all remaining actuations are performed as planned.

Finally, due to the absence of direct measurements of motor limits through force or tension sensors, a simple motor limit mapping strategy was implemented to prevent the control system from entering actuation saturation. This approach is based on tracking the number of admissible actuation steps in the anterior, posterior, and medial directions.
Starting from a fully relaxed tendon configuration, the available actuation range for each direction was identified offline by incrementally commanding motor steps until the corresponding actuation limit was reached. These values were stored and subsequently used as reference bounds during online control.
At the beginning of each control execution, the system detects whether a given actuation direction is feasible by issuing a small exploratory command and evaluating the resulting displacement using the same thresholding strategy described above. In particular, the catheter is moved out of the insertion and AP dead-zone regions, and the Euclidean distance between the EMA-filtered position before and after the actuation is computed. when movement is detected, the remaining number of admissible actuation steps in that direction is updated accordingly.

Once the pre-identified actuation limit is reached for a given direction, further commands exceeding that limit are inhibited, and the control loop continues by considering only the remaining feasible actuation directions. In this way, the system prevents invalid actuation commands without requiring direct force or tension measurements, while maintaining stable operation of the Jacobian update and control algorithms.

3.5. Stability Analysis

The stability of the proposed control strategy is analyzed using Lyapunov theory [71]. Let

$$\boldsymbol{E} = \bar{\boldsymbol{p}}^{tip} - \boldsymbol{p}^{tip} \in \mathbb{R}^3 \tag{53}$$

denote the task-space tracking error, where $\bar{\boldsymbol{p}}^{tip}$ is the desired target position and $\boldsymbol{p}^{tip}$ is the current tip position. Within each control interval, the target point computed by MPP can be considered as constant, i.e.

$$\dot{\bar{\boldsymbol{p}}}_t = 0, \tag{54}$$

thus,

$$\dot{\boldsymbol{E}}_t = -\dot{\boldsymbol{p}}_t. \tag{55}$$

Since $\hat{\boldsymbol{J}}$ (from now on $\boldsymbol{J}$) is square and full rank, from Eq.(45), we can retrieve that

$$\dot{\boldsymbol{p}}_t = \boldsymbol{J}^{-1}\dot{\boldsymbol{q}}_t, \tag{56}$$

hence the error dynamics can be written as

$$\dot{\boldsymbol{E}}_t = -\boldsymbol{J}^{-1}\dot{\boldsymbol{q}}_t. \tag{57}$$

Consider the quadratic Lyapunov function

$$V(\boldsymbol{E}) = \frac{1}{2}\boldsymbol{E}^\top \boldsymbol{E} \geq 0. \tag{58}$$

Its time derivative is

$$\dot{V}(\boldsymbol{E}) = \boldsymbol{E}^\top \dot{\boldsymbol{E}} = -\boldsymbol{E}^\top \boldsymbol{J}^{-1}\dot{\boldsymbol{q}}. \tag{59}$$

We set [72]

$$\dot{\boldsymbol{E}}_t = -\alpha \boldsymbol{E}_t, \qquad \alpha > 0. \tag{60}$$

Combining this relation with Eq.57 yields

$$-\alpha \boldsymbol{E}_t = -J^{-1}\dot{q}_t \;\Rightarrow\; \boldsymbol{E}_t = \frac{1}{\alpha}\boldsymbol{J}^{-1}\dot{\boldsymbol{q}}_t, \tag{61}$$

where $\alpha > 0$. Replacing $\boldsymbol{E}_t = \frac{1}{\alpha}\boldsymbol{J}^{-1}\dot{\boldsymbol{q}}_t$ into $\dot{V}(E)$ we obtain

$$\dot{V}(\boldsymbol{E}) = -\frac{1}{\alpha}\dot{\boldsymbol{q}}^\top (\boldsymbol{J}^{-1})^T \boldsymbol{J}^{-1}\dot{\boldsymbol{q}} \leq 0, \tag{62}$$

To account for Jacobian mismatch and unmodeled effects, we introduce an equivalent bounded disturbance term in the error dynamics:

$$\dot{\boldsymbol{E}}_t = -\boldsymbol{J}^{-1}\dot{\boldsymbol{q}}_t + \boldsymbol{\omega}_t, \qquad \|\boldsymbol{\omega}_t\| \leq \xi \tag{63}$$

where ξ is a normal constant. Eq. (62) becomes

$$\dot{V}(E) = -\frac{1}{\alpha}\dot{\boldsymbol{q}}^\top (\boldsymbol{J}^{-1})^\top \boldsymbol{J}^{-1}\dot{\boldsymbol{q}} + \boldsymbol{\omega}^\top \boldsymbol{J}^{-1}\dot{\boldsymbol{q}}. \tag{64}$$

In this scenario, if $\dot{V}(\boldsymbol{E}) < 0$, then the Lyapunov function decreases and the tracking error $\boldsymbol{E}$ is driven toward the origin. Otherwise, if $\dot{V}(\boldsymbol{E}) \geq 0$, then

$$\dot{V}(\boldsymbol{E}) = -\frac{1}{\alpha}\dot{\boldsymbol{q}}^\top (J^{-1})^\top \boldsymbol{J}^{-1}\dot{\boldsymbol{q}} + \frac{1}{\alpha}\boldsymbol{\omega}^\top \boldsymbol{J}^{-1}\dot{\boldsymbol{q}}. \tag{65}$$

Using the Cauchy–Schwarz inequality,

$$\boldsymbol{\omega}^\top \boldsymbol{J}^{-1}\dot{\boldsymbol{q}} \leq \|\boldsymbol{\omega}\|_2 \, \|\boldsymbol{J}^{-1}\dot{\boldsymbol{q}}\|_2, \tag{66}$$

So finally we have

$$\|\boldsymbol{E}_t\| \leq \|\boldsymbol{\omega}\|_2 \leq \xi. \tag{67}$$

We can then conclude, from the two cases above, that the tracking error decreases when $\dot{V} < 0$ and remains bounded when $\dot{V} \geq 0$.

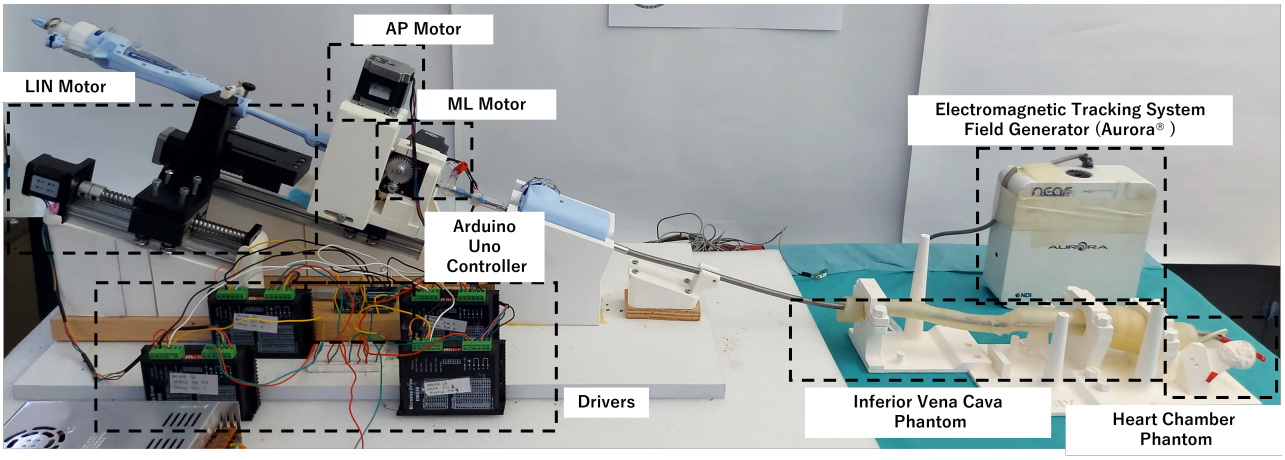

Figure 13: Caption

4. Experimental Setting and Experimental Protocol

The experimental pipeline aims to evaluate the performance of the proposed ultrasound-driven predictive targeting framework when applied to a tendon-driven CR performing dynamic target reaching of a mitral-valve-like structure oscillating with physiological kinematics. The experiments specifically assess:

- Fidelity of the MAPSE-based valve-motion generator,
- Accuracy of the predicted target trajectory,
- Robot tracking performance under dynamic target motion,
- Contribution of each algorithmic component (EKF prediction, MPTP, Jacobian adaptation) via ablation studies.

4.1. MAPSE Extraction from US

For MAPSE estimation and mitral valve annulus tracking, a training dataset composed of 1,526 videos and a total of 45,672 frames was used, derived from the EchoNet-Dynamic dataset [73]. For each video, manual ventricular annotations were available only at end-diastole (ED) and end-systole (ES), corresponding to the contraction and relaxation phases of the cardiac cycle. The remaining frames were obtained by propagating the annulus landmarks throughout the cardiac cycle using Lucas–Kanade optical flow. The resulting dataset was split on a frame basis into 80% training, 10 % validation, and 10% test sets. The YOLO-Pose network was trained on a standard laptop computer (ThinkPad) without GPU acceleration for 50 epochs, using a mini-batch size of 64 frames and an input resolution of 128 $\times$ 128 pixels. During inference, keypoint detections were considered valid only if their confidence score exceeded a predefined threshold of 0.25, representing the minimum confidence required to accept a prediction. Low-confidence detections were discarded, and temporal consistency was enforced by retaining the last valid prediction when detections were missing.

4.2. Testbed Validation

The proposed method was validated using a comprehensive testbed setup, shown in Figure **??**. The setup includes the following components: Catheter testbench setup:

- The CR under study, obtained by motorizing the Mitraclip^{TM} system (Abbott Vascular, CA, USA).
- Two 6-DoF EM sensors (Aurora, NDI, Canada) attached at the tip and at the base on the outer CR, providing continuous measurements at 40 Hz.
- Two Nema 23 stepper motors (JoyNano) are utilized to actuate the pulleys connected to tendons, allowing for the bending of the CR in both the ML and AP planes.
- One linear actuator Nema 17 Bipolar Stepper Motor (Sainsmart) for moving the tip in the forward direction (LIN).
- An anatomical phantom is derived from patient-specific CT scans simulating the inferior vena cava, interatrial septum, and mitral valve.
- Each motor was controlled by a DM556 driver (Jadeshay) and connected to an Arduino Uno microcontroller sending control commands at a frequency of 10 Hz.

Valve testbench setup:

- One BE069-4 linear actuator with a Nema 17 Bipolar Stepper Motor (Befenybay, USA) for moving the valve in a specific direction.
- A 3-D printed arm designed to move the 6-DoF sensor away from the electromagnetic interferences of the motor
- One 6-DoF EM sensors (Aurora, NDI, Canada) attached to the 3-D printed arm providing continuous measurements at 10 Hz to mimic a realistic Neural Network estimated MV position.
- The motor was controlled by a TB6600 (QWORK®) driver and connected to an Arduino Nano RP2040 Connect microcontroller sending the steps to move the motor to replicate the extracted sinusoid obtained at 4.1.

The Robotic Operating System (ROS) served as the integration framework, facilitating communication and coordination among the various components of the setup.

4.3. Experimental Protocol

To evaluate the performance of the proposed approach, two distinct batches of experimental tests were conducted, addressing complementary aspects of control performance and robustness.

Performance Test. In the first batch of experiments, the proposed Task-Space Jacobian Update approach (TS-JUPD) was compared against two baseline methods. The first baseline is a classical Model Predictive Control formulation using an analytical Jacobian (MPC), described in Section 2.4. The second baseline corresponds to the control strategy presented in Section 3, where the adaptive optimization algorithm described in Section 3.3 is replaced by an analytical Jacobian derived from the Constant Curvature model and a Proportional–Derivative controller in task space (TS-PD), as described in Section 2.3.2. The PD controller gains were empirically tuned in order to achieve the best possible tracking performance.
Specifically, the capability of each method to track a dynamic target was evaluated. The target motion was generated in software by simulating the ideal mitral valve behavior as an unperturbed double-sinusoidal trajectory. Six distinct target locations were selected within the catheter workspace. These locations were identified by manually steering the catheter to different regions of the workspace, with the aim of covering a wide range of tendon configurations.
To reduce statistical variability across trials and to mitigate bias due to progressive tendon wear, the experiments were executed following an interleaved protocol. One observation consisting of six target points was collected for the TS-JUPD method, followed by one observation of six points for the TS-PD method. This sequence was repeated four times, resulting in a total of 24 observations per method, while ensuring a comparable level of mechanical wear across all trials. Subsequently, the MPC method was evaluated following the same data collection protocol. This experimental batch is hereafter referred to as the *Performance Test*.

Robustness Test. In the second batch of experiments, only the method achieving the best performance according to the evaluation metrics defined in Section 4.3.1 was further assessed. This batch aimed to evaluate the robustness of the control strategy under varying target dynamics and model uncertainties.
In this case, dynamic valve position data were generated using the simulated valve motion produced by the linear motor described previously. Target points were selected to generate trajectories of comparable length and complexity to those typically executed by an expert surgeon, thereby approximating realistic clinical operating conditions. The objective was to assess the robustness of the valve motion estimation and control performance in the presence of noise and model inaccuracies.
Variations in both MAPSE amplitude and oscillation frequency were introduced within physiological ranges, namely MAPSE $\in \{6\,\text{mm}, 6.5\,\text{mm}, 7\,\text{mm}\}$ and frequency $\in \{1\,\text{Hz}, 1.15\,\text{Hz}, 1.3\,\text{Hz}\}$. To limit the total number of experiments, only the paired combinations [6 mm, 1 Hz], [6.5 mm, 1.15 Hz], and [7 mm, 1.3 Hz] were considered. For each point–amplitude–frequency triplet, the control experiment was repeated four times, resulting in a dataset of 36 observations. This second batch of experiments is referred to as the *Robustness Test*.

Horizon Test Furthermore, a test to explore the effect of different prediction horizons on the overall time to reach the target was carried out. 6 runs on 1 point were evaluated for each prediction horizon (2, 3, 5, 7, 10, 15).

4.3.1. Evaluation Metrics

For the evaluation of the proposed control method, the following performance metrics were collected:

- Success Rate (SR) [%]: A trial is considered successful if the target is reached within a maximum allowed time $T_{\max} = 600$ s, with a maximum admissible error $\varepsilon = 0.98$ mm, corresponding to the accuracy of the EM sensing system. The success rate is then defined as

$$\mathrm{SR} = \frac{N_{\mathrm{succ}}}{N} \times 100, \tag{68}$$

  where N_{succ} is the number of successful trials and N is the total number of trials.
- Trajectory Length (TL) [mm]: For each successful trial, the trajectory length of the CR's tip ($\boldsymbol{p}_{CR}$), computed up to the target reaching time, is

$$TL = \sum_{k=1}^{K-1} \left\| \boldsymbol{p}_{CR}(t_{k+1}) - \boldsymbol{p}_{CR}(t_k) \right\|_2, \tag{69}$$

  where K is the index corresponding to t_{reach}.
- Control loop Time (CT) [s]: For each successful trial, CT is defined as the time interval between two consecutive control outputs computed by the controller:

$$CT = t_{k+1} - t_k \tag{70}$$

  where t_k^{cmd} denotes the time at which the k-th control command is published.
- Time to Target (TT) [s]: For each successful trial, the TT is computed as the elapsed time between the start of the trial and the first instant at which the target is reached.
- **Time to go under a given threshold ($\mathbf{TUT}_X$) [s]**: For each trial, TUT_X is defined as the time required for the Euclidean distance between the target position and the measured tip position to fall below a predefined threshold X [mm], i.e.,

$$\|\overline{\mathbf{p}}^{\mathrm{tip}} - \mathbf{p}^{\circ,\mathrm{tip}}(t)\|_2 < X. \tag{71}$$

  An important observation must be done regarding the MPC. Due to it's formulation, the MPC model is not feasible to be evaluated using this metric. in fact, the output of the controller are already the control actions. therefore no evaluation is possible using this metric.

Statistical analysis was performed on the considered performance metrics. Results are reported using the mean and interquartile range (IQR). For SR, statistical significance was assessed using Fisher's exact test. Upon verifying the non-normality of the data distribution through a Shapiro-Wilk test, the Kruskal-Wallis non-parametric test was applied at a significance level of 0.05 or 0.01. The analysis was carried out in Python, using the scipy library.

5. Results and Discussion

With reference to the *Performance Test* described in Section 4.3, the success rate (SR) achieved by the MPC baseline was 54.17%, while the TS-PD approach achieved an SR of 75%. In contrast, the proposed TS-JUPD method achieved a success rate of 100%, demonstrating a clear performance advantage over the two baseline approaches. In addition, the average time-to-target (TT) further highlights this superiority. The TS-JUPD method achieved an average TT of 242.26 s, compared to 360.03 s for MPC and 374.98 s for TS-PD. These results indicate that the proposed method outperforms both baseline strategies in terms of reliability and convergence speed.

The statistical significance of the success rate results was evaluated using Fisher's exact test. The analysis revealed a statistically significant difference between TS-JUPD and TS-PD ($p < 0.05$), whereas no statistically significant difference was observed between TS-PD and MPC ($p < 0.05$). This finding suggests that the improvement in SR is specifically attributable to the online Jacobian update mechanism introduced in TS-JUPD. The time-to-target distributions were subsequently analyzed using a three-sample Kruskal–Wallis test, yielding a statistically significant result ($F = 25.33$, p-value < 0.01). Following this outcome, a post-hoc Dunn test with Bonferroni correction was applied. The post-hoc analysis identified statistically significant differences in TT only between TS-JUPD and the two baseline methods ($p < 0.01$), while no significant difference was detected between TS-PD and MPC. These results confirm the statistical significance of the performance improvement achieved by the proposed method.

In terms of motion efficiency, TS-JUPD produces significantly shorter trajectories compared to MPC ($p < 0.01$) and TS-PD ($p < 0.01$). Consequently, the proposed approach also achieves the lowest total time to reach the target, with a statistically significant improvement over TS-PD ($p < 0.01$). These results show that the proposed approach consistently improves task-level performance. As expected, the minimum computation

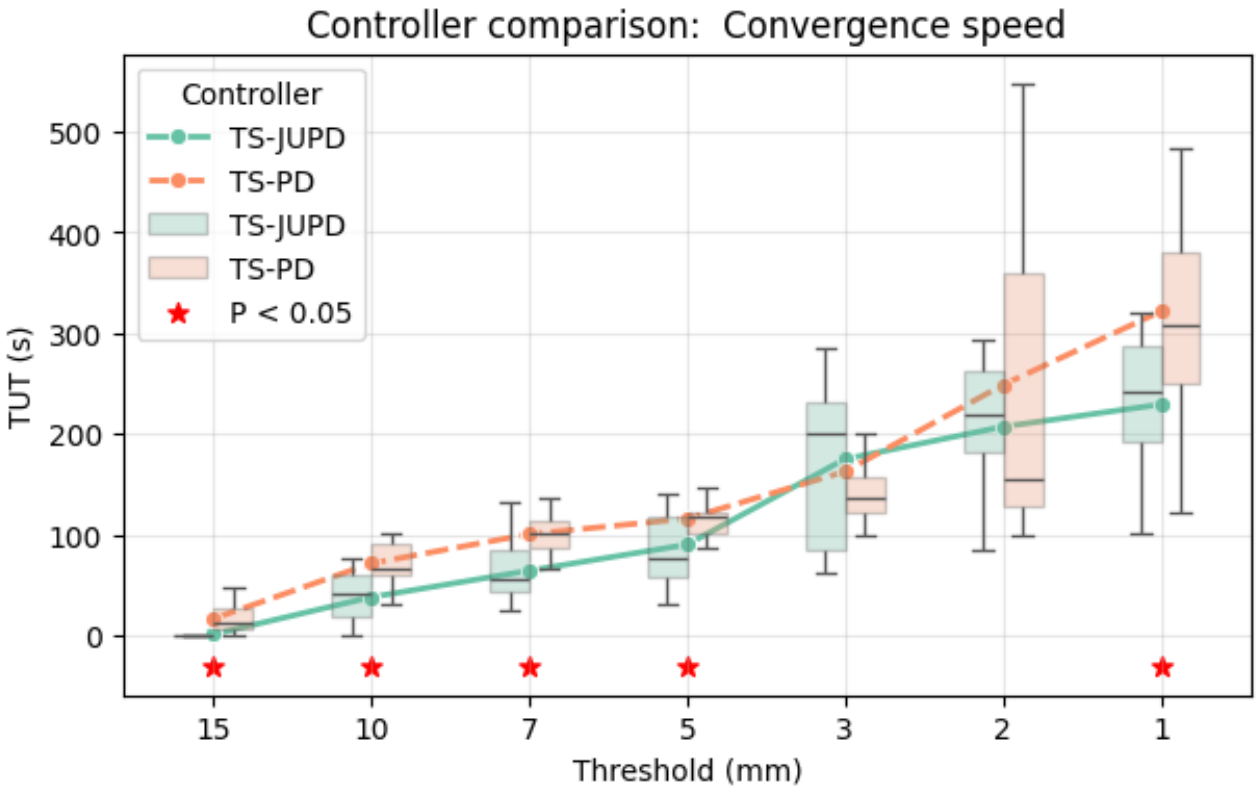

Figure 14: Distribution of time-to-target values required to reach different trajectory position error thresholds for the compared control strategies. Red markers indicate statistically significant differences between distributions.

Table 3: Comparison between MPC, TS-PD, and the proposed TS-JUPD approach in the first set of experiments. Results are reported as mean ± standard deviation. for MPC TUT_X are not available (N.A.). Best results are highlighted in ***BOLD***

Method	**SR [%]**	**CT [s]**	**TT [s]**	**TUT_5 [s]**	**TUT_1 [s]**	**TL [mm]**
MPC	55	6.0 ± 3.0	360 ± 60	N.A.	N.A.	100 ± 10
TS-PD	75	$\mathbf{2.3 \pm 0.3}$	375 ± 40	116.11 ± 17.72	321.67 ± 101.22	88 ± 6
TS-JUPD	**100**	7.4 ± 2.8	$\mathbf{260 \pm 45}$	$\mathbf{90.36 \pm 46.28}$	$\mathbf{229.38 \pm 66.64}$	$\mathbf{72 \pm 6}$

time is achieved by the TS-PD controller, which relies on an algebraic control law and therefore entails a very low computational cost. However, although TS-JUPD does not minimize CT, the increased accuracy in the kinematic mapping enabled by the continuous Jacobian update leads to more feasible and efficient trajectories, as well as more effective control execution. This results in a reduction of the total time to reach the target and an improvement in the success rate.

Further insight into the convergence properties of the control strategies can be obtained by analyzing the time required to reduce the trajectory position error below predefined thresholds (TUT). Kruskal–Wallis tests were performed on the distributions of TUT thresholds of 15, 10, 7, 5, 3, 2, and 1 mm. The analysis shows that TS-JUPD converges significantly faster than the baseline methods for thresholds of 15, 10, 7, 5, and 1 mm, indicating superior adaptability and convergence behavior compared to a classical PD-based control strategy.

These results are visually summarized in Fig. 14, which reports the distribution of times required to reach different trajectory error thresholds. The mean TUT values associated with TS-JUPD are consistently lower across all thresholds except for 3 mm. Red markers indicate statistically significant differences between distributions. Moreover, for the most stringent thresholds of 2 and 1 mm, the interquartile range (IQR) of the TS-JUPD method is substantially narrower than that of TS-PD. This observation suggests a more consistent and fine-grained control behavior of the proposed method when operating close to the target, highlighting the benefits of online Jacobian adaptation in high-precision tracking tasks.

Table 4: Robustness analysis of the proposed control approach under increasing frequency of the sinusoidal input applied to the linear stage. Results are reported as mean ± standard deviation.

f [Hz]	**SR [%]**	**CT [s]**	**TT [s]**	**TL [mm]**
1.0	100 ± 0	2.7 ± 0.9	185 ± 28	52 ± 5
1.15	100 ± 0	2.5 ± 2.5	200 ± 22	54 ± 7
1.3	100 ± 0	2.8 ± 1.3	180 ± 35	55 ± 8

Table 5: Horizon Test analysis of the proposed control approach Variable Horizon N. Results are reported as mean ± standard deviation.

N	**SR [%]**	**CT [s]**	**TT [s]**	**TL [mm]**
2	100 ± 0	2.7 ± 0.9	185 ± 28	52 ± 5
5	100 ± 0	2.5 ± 2.5	200 ± 22	54 ± 7
10	100 ± 0	2.8 ± 1.3	180 ± 35	55 ± 8
15	100 ± 0	2.8 ± 1.3	180 ± 35	55 ± 8

With reference to the *Robustness Test* described in Section 4.3, the proposed control strategy failed to reach the target in only one experimental trial. Overall, no statistically significant differences were observed across the analyzed performance metrics when comparing the different amplitude–frequency pairs. This result confirms the robustness of both the valve position estimation algorithm and the associated trajectory planning strategy with respect to variations in oscillation amplitude and frequency within physiological ranges.
A closer inspection of the failed trial indicates that the issue did not stem from a control or planning inaccuracy, but rather from actuation constraints. Due to the extremely posterior initial location of the target relative to the catheter starting configuration, the posterior tendon reached its actuation limit at an early stage of the maneuver. As described in Section 3.4, once a tendon limit is detected, further actuation in that direction is inhibited to prevent mechanical overstress.
Although subsequent catheter insertions induced a partial relaxation of the posterior tendon, the absence of direct tendon tension sensing prevented the controller from detecting this change in actuation availability. Consequently, posterior actuation was not re-enabled, despite being physically admissible according to the actual tendon state and the trajectory planner requirements. The failure can therefore be attributed to conservative operational boundary management rather than to inaccuracies in Jacobian estimation or model identification.
The robustness analysis results are summarized in Tab. 4, which reports the performance metrics across the tested amplitude and frequency conditions.
Concerning the *Horizon Test*, the analyzed metrics revealed a statistically significant difference only in the Completion Time (CT) metric (see Table 5), with $N = 10$ yielding the lowest value. However, this result should be interpreted with caution, as CT is not particularly informative in this context.
Due to the absence of feedback regarding the effective completion of motor actuation by the drivers, the dominant source of delay between successive MPTP outputs was the intrinsic motor response time. As a consequence, larger prediction horizons (N) generated task-space references that were closer to the target position, resulting in smaller actuation increments. This reduced the number of required control updates and, indirectly, the cumulative motor delay. Therefore, the observed reduction in CT for higher N values can be considered partially structural rather than purely performance-related.
Although not statistically significant, $N = 10$ also exhibited a lower Tendon Load (TL). This trend suggests a potential improvement in actuation efficiency for larger prediction horizons, which should be further investigated through a larger experimental campaign to draw definitive conclusions.

6. Conclusions and Future Developments

This work investigated the feasibility of performing position control on a dynamically moving target using a tendon-driven continuum robot, with specific application to mitral valve intervention. The study addressed both the modeling and control challenges arising from the intrinsic nonlinearities of continuum manipulators and from the presence of physiologically realistic target motion.

The proposed task-space control strategy, based on an Online-Estimated Jacobian, demonstrated the capability to adapt the kinematic mapping between actuation space and task space in real time. By continuously updating the Jacobian through a data-driven Least-Squares formulation, the controller was able to compensate for configuration-dependent nonlinearities, tendon hysteresis, dead zones, and catheter-to-catheter variability. Experimental results showed improved kinematic consistency, more efficient trajectories, and superior task-level performance compared to baseline approaches. Moreover, the method proved robust under non-ideal scenarios, including variations in target oscillation frequency and amplitude within physiological ranges.

Despite these promising results, several limitations remain. First, the mitral valve (MV) motion model currently adopted provides only a first-order approximation of the actual valve dynamics. While sufficient to validate the control framework, a more accurate representation incorporating patient-specific kinematics or higher-order dynamic effects would likely increase the fidelity of the testing environment, ultimately assessing the full clinical transferability of the control framework into the clinical practice.

Second, the current Model Predictive Trajectory Planner (MPTP) focuses primarily on minimizing positional tracking error without explicitly considering geometric optimality of the approach. Future developments may include the introduction of an additional cost term promoting orthogonality between the catheter tip orientation and the instantaneous valve motion direction. For example, constraining the terminal segment of the trajectory to be orthogonal to the MAPSE direction could encourage a more physiologically favorable approach configuration. Although such a constraint would not enforce perfect orthogonality along the entire trajectory, it would bias the planner toward safer and more effective insertion strategies.

Furthermore, preliminary experimental observations suggest that adopting a Variable Prediction Horizon within the MPTP could improve performance, particularly in terms of Task Time (TT). A dynamically adjusted horizon, modulated according to the instantaneous state of both the valve and the catheter, would allow the planner to better anticipate rapid motion changes while avoiding unnecessary computational burden in quasi-static phases. Such an adaptive strategy could enhance responsiveness to target dynamics, increase trajectory feasibility, and prevent over-constraining the underlying optimization problem.

Finally, the experimental campaign highlighted the importance of actuation boundary management in tendon-driven systems. Future work should therefore address the integration of tendon tension sensing or state observers capable of detecting tendon relaxation phenomena through the introduction of tension sensors on the motors. This would allow dynamic re-enablement of previously saturated actuation directions and further improve robustness in extreme configurations.

In conclusion, the presented framework demonstrates that adaptive task-space control combined with predictive trajectory planning constitutes a viable and robust strategy for interacting with dynamically moving anatomical targets using continuum robots. The proposed methodology provides a solid foundation for future translational developments toward clinically relevant robotic mitral valve interventions.

References

[1] World Health Organization. Cardio vascular diseases. `https://www.who.int/news-room/fact-sheets/detail/cardiovascular-diseases-(cvds)`, 2025. Accessed: Jan. 2026.

[2] European Heart network. European cardiovascular disease statistics 2017. `https://ehnheart.org/library/cvd-statistics/european-cardiovascular-disease-statistics-2017/`, 2017. Accessed: Jan. 2026.

[3] Gaetano Santulli. Epidemiology of cardiovascular disease in the 21st century: Updated numbers and updated facts. *Journal of cardiovascular disease research*, 1:1, 07 2013.

[4] Maurice Enriquez-Sarano, Cary W Akins, and Alec Vahanian. Mitral regurgitation. *The Lancet*, 373(9672):1382–1394, 2009.

[5] Romain Capoulade, Nicolas Piriou, Jean-Michel Serfaty, and Thierry Le Tourneau. Multimodality imaging assessment of mitral valve anatomy in planning for mitral valve repair in secondary mitral regurgitation. *Journal of Thoracic Disease*, 9(Suppl 7), 2017.

[6] Jacob P. Dal-Bianco, Elena Aikawa, Joyce Bischoff, J. Luis Guerrero, Mark D. Handschumacher, Suzanne Sullivan, Benjamin Johnson, James S. Titus, Yoshiko Iwamoto, Jill Wylie-Sears, Robert A. Levine, and Alain Carpentier. Active adaptation of the tethered mitral valve. *Circulation*, 120(4):334–342, 2009.

[7] Alec, Ottavio Alfieri, Felicita Andreotti, Manuel J Antunes, Gonzalo Barón-Esquivias, Helmut Baumgartner, Michael Andrew Borger, Thierry P Carrel, Michele De Bonis, et al. Guidelines on the management of valvular heart disease (version 2012) the joint task force on the management of valvular heart disease of

the european society of cardiology (esc) and the european association for cardio-thoracic surgery (eacts). *European heart journal*, 33(19):2451–2496, 2012.

[8] Henryk Welp and Sven Martens. Minimally invasive mitral valve repair. *Current Opinion in Anaesthesiology*, 27(1):65–71, 2014.

[9] K Holmes, B Gibbison, and H A Vohra. Mitral valve and mitral valve disease. *BJA Education*, 17(1):1–9, 2017.

[10] Karen P. McCarthy, Liam Ring, and Bushra S. Rana. Anatomy of the mitral valve: understanding the mitral valve complex in mitral regurgitation. *European Journal of Echocardiography*, 11(10):i3–i9, 12 2010.

[11] The Keyhole Heart Clinic. `https://www.thekeyholeheartclinic.com/services/valve-disorders/mitral-valve2/mitral-regurgitation/`. Accessed: Jan. 2026.

[12] Jeffrey Shuhaiber and Robert J. Anderson. Meta-analysis of clinical outcomes following surgical mitral valve repair or replacement. *European Journal of Cardio-Thoracic Surgery*, 31(2):267–275, 02 2007.

[13] Robert R. Moss, Karin H. Humphries, Min Gao, Christopher R. Thompson, James G. Abel, Guy Fradet, and Brad I. Munt. Outcome of mitral valve repair or replacement: A comparison by propensity score analysis. *Circulation*, 108(10_suppl_1):II–90–II–97, 2003.

[14] Stephanie L. Mick, Suresh Keshavamurthy, and A. Marc Gillinov. Mitral valve repair versus replacement. *Annals of Cardiothoracic Surgery*, 4(3), 2015.

[15] L.A. McKeown. `https://www.tctmd.com/news/sts-data-mitral-valve-cases-are-fastest-growing-cv-surgica` Accessed: Jan. 2026.

[16] Diagnostic and Interventional Cardiology. `https://www.dicardiology.com/article/treating-mitral-regurgitation-high-risk-patients`. Accessed: Jan. 2026.

[17] Davy C. H. Cheng, Janet Martin, Avtar Lal, Anno Diegeler, Thierry A. Folliguet, L. Wiley Nifong, Patrick Perier, Ehud Raanani, J. Michael Smith, Joerg Seeburger, and Volkmar Falk. Minimally invasive versus conventional open mitral valve surgery a meta-analysis and systematic review. *Innovations*, 6(2):84–103, 2011. PMID: 22437892.

[18] Ilias P. Doulamis, Eleftherios Spartalis, Nikolaos Machairas, Dimitrios Schizas, Dimitrios Patsouras, Michael Spartalis, Diamantis I. Tsilimigras, Demetrios Moris, Dimitrios C. Iliopoulos, Aspasia Tzani, Dimitrios Dimitroulis, and Nikolaos I. Nikiteas. The role of robotics in cardiac surgery: a systematic review. *Journal of Robotic Surgery*, 13(1):41–52, 2019.

[19] Paul Sorajja, João L. Cavalcante, Mario Gossl, and Richard Bae. Transcatheter repair of tricuspid regurgitation with mitraclip. *Progress in Cardiovascular Diseases*, 62(6):488–492, 2019.

[20] Ilkay Bozdag-Turan, Liliya Paranskaya, Ralf Birkemeyer, Gökmen R. Turan, Stephan Kische, Ibrahim Akin, Jasmin Ortak, Yannik Stoeckicht, Jochen Schubert, Bernd Westphal, Christoph A. Nienaber, and Hüseyin Ince. Percutaneous mitral repair with the mitraclip system in patients with mild-to-moderate and severe heart failure: A single-centre experience. *Cardiovascular Therapeutics*, 32(2):66–73, 2014.

[21] Ted Feldman, Saibal Kar, Michael Rinaldi, Peter Fail, James Hermiller, Richard Smalling, Patrick L. Whitlow, William Gray, Reginald Low, Howard C. Herrmann, Scott Lim, Elyse Foster, and Donald Glower. Percutaneous mitral repair with the mitraclip system: Safety and midterm durability in the initial everest (endovascular valve edge-to-edge repair study) cohort. *Journal of the American College of Cardiology*, 54(8):686–694, 2009.

[22] Aswin Srinivasan, Jonathan Brown, Haris Ahmed, and Michael Daniel. Pascal repair system for patients with mitral regurgitation: A systematic review. *International Journal of Cardiology*, 376:108–114, 2023.

[23] Abott Cardiovascular. `https://www.cardiovascular.abbott/us/en/hcp/products/structural-heart/transcatheter-valve-solutions.html`. Accessed: Jan. 2026.

[24] Ottavio Alfieri, Francesco Maisano, Michele De Bonis, Pier Luigi Stefano, Lucia Torracca, Michele Oppizzi, and Giovanni La Canna. The double-orifice technique in mitral valve repair: A simple solution for complex problems. *The Journal of Thoracic and Cardiovascular Surgery*, 122(4):674–681, 2001.

[25] Michael J. Mack, William T. Abraham, JoAnn Lindenfeld, Steven F. Bolling, Ted E. Feldman, Paul A. Grayburn, Samir R. Kapadia, Patrick M. McCarthy, D. Scott Lim, James E. Udelson, Michael R. Zile, James S. Gammie, A. Marc Gillinov, Donald D. Glower, David A. Heimansohn, Rakesh M. Suri, Jeffrey T. Ellis, Yu Shu, Saibal Kar, Neil J. Weissman, and Gregg W. Stone. Cardiovascular outcomes assessment of the mitraclip in patients with heart failure and secondary mitral regurgitation: Design and rationale of the coapt trial. *American Heart Journal*, 205:1–11, 2018.

[26] M. Sherif, L. Paranskaya, Seyrani Yuecel, Stephan Kische, O. Thiele, G. D'Ancona, A. Neuhausen-Abramkina, Jasmin Ortak, Haluk Ince, and Alper Öner. Mitraclip step by step; how to simplify the procedure. *Netherlands Heart Journal*, 25, 12 2016.

[27] A.P. Patrianakos, A.A. Zacharaki, E.I. Skalidis, M.I. Hamilos, F.I. Parthenakis, and P.E. Vardas. The growing role of echocardiography in interventional cardiology: The present and the future. *Hellenic Journal of Cardiology*, 58(1):17–31, 2017.

[28] A. Kataoka, Y. Watanabe, and O.-S. Family. Mitraclip: a review of its current status and future perspectives. *Cardiovascular Intervention and Therapeutics*, pages 1–11, 2022.

[29] G. Nickenig, R. Estevez-Loureiro, O. Franzen, C. Tamburino, M. Vanderheyden, T. F. Lüscher, N. Moat, S. Price, G. Dall'Ara, R. Winter, et al. Percutaneous mitral valve edge-to-edge repair: in-hospital results and 1-year follow-up of 628 patients of the 2011–2012 pilot european sentinel registry. *Journal of the American College of Cardiology*, 64(9):875–884, 2014.

[30] F. Maisano, M. Taramasso, M. Cioni, N. Buzzatti, P. Denti, A. Colombo, and O. Alfieri. Review of the mitraclip clinical evidence. *Minerva Cardioangiologica*, 60(1):85–93, 2012.

[31] K. Vakil, H. Roukoz, M. Sarraf, B. Krishnan, M. Reisman, W. C. Levy, and S. Adabag. Safety and efficacy of the mitraclip® system for severe mitral regurgitation: a systematic review. *Catheterization and Cardiovascular Interventions*, 84(1):129–136, 2014.

[32] S. Alsidawi, M. Effat, and T. Helmy. Advances in interventional cardiology: Mitraclip. *Journal of Thrombosis and Thrombolysis*, 38:260–268, 2014.

[33] Francesco Maisano, Olaf Franzen, Stephan Baldus, Ulrich Schäfer, Jörg Hausleiter, Christian Butter, Gian Paolo Ussia, Horst Sievert, Gert Richardt, Julian D. Widder, Tiziano Moccetti, and Wolfgang Schillinger. Percutaneous mitral valve interventions in the real world: Early and 1-year results from the access-eu, a prospective, multicenter, nonrandomized post-approval study of the mitraclip therapy in europe. *Journal of the American College of Cardiology*, 62(12):1052–1061, 2013.

[34] Mackram F. Eleid, Guy S. Reeder, Joseph F. Malouf, Ryan J. Lennon, Sorin V. Pislaru, Vuyisille T. Nkomo, and Charanjit S. Rihal. The learning curve for transcatheter mitral valve repair with mitraclip. *Journal of Interventional Cardiology*, 29(5):539–545, 2016.

[35] A. K. Chhatriwalla, S. Vemulapalli, D. R. Holmes Jr, D. Dai, Z. Li, G. Ailawadi, D. Glower, S. Kar, M. J. Mack, J. Rymer, and et al. Institutional experience with transcatheter mitral valve repair and clinical outcomes: insights from the tvt registry. *Cardiovascular Interventions*, 12(14):1342–1352, 2019.

[36] J. E. Boland, L. W. Wang, B. J. Love, D. G. Wynne, and D. W. Muller. Radiation dose during percutaneous treatment of structural heart disease. *Heart, Lung and Circulation*, 23(11):1075–1083, 2014.

[37] Z. K. Wegermann, R. V. Swaminathan, and S. V. Rao. Cath lab robotics: paradigm change in interventional cardiology? *Current Cardiology Reports*, 21:1–7, 2019.

[38] Dan-Mihai Rusu, Silviu-Dan Mândru, Cristina-Maria Biriș, Olivia-Laura Petrașcu, Fineas Morariu, and Alexandru Ianosi-Andreeva-Dimitrova. Soft robotics: A systematic review and bibliometric analysis. *Micromachines*, 14(2), 2023.

[39] Tomas da Veiga, James H Chandler, Peter Lloyd, Giovanni Pittiglio, Nathan J Wilkinson, Ali K Hoshiar, Russell A Harris, and Pietro Valdastri. Challenges of continuum robots in clinical context: a review. *Progress in Biomedical Engineering*, 2(3):032003, jul 2020.

[40] Jessica Burgner-Kahrs, D. Caleb Rucker, and Howie Choset. Continuum robots for medical applications: A survey. *IEEE Transactions on Robotics*, 31(6):1261–1280, 2015.

[41] K. H. Fuchs. Minimally invasive surgery. *Endoscopy*, 34(2):154–159, 2002.

[42] Valentina Vitiello, Su-Lin Lee, Thomas P. Cundy, and Guang-Zhong Yang. Emerging robotic platforms for minimally invasive surgery. *IEEE Reviews in Biomedical Engineering*, 6:111–126, 2013.

[43] Jessica Burgner-Kahrs, D. Rucker, and Howie Choset. Continuum robots for medical applications: A survey. *IEEE Transactions on Robotics*, 31:1–20, 11 2015.

[44] Michelle Mattille, Quentin Boehler, Jonas Lussi, Nicole Ochsenbein, Ueli Moehrlen, and Bradley J. Nelson. Autonomous magnetic navigation in endoscopic image mosaics. *Advanced Science*, 11(19):2400980, 2024.

[45] Xiu Zhang, Maria Chiara Palumbo, Francesca Perico, Mattia Magro, Andrea Fortuna, Tommaso Magni, Emiliano Votta, Alice Segato, and Elena De Momi. Robotic actuation and control of a catheter for structural intervention cardiology. In *2022 IEEE/RSJ International Conference on Intelligent Robots and Systems (IROS)*, pages 5907–5913, 2022.

[46] X. Zhang, A. Sridhar, X. T. Ha, S. Z. Mehdi, A. Fortuna, M. Magro, A. Peloso, A. Bicchi, M. Ourak, and A. Aliverti. Path tracking control of a steerable catheter in transcatheter cardiology interventions. *International Journal of Computer Assisted Radiology and Surgery*, 19(4):757–766, 2024.

[47] G. Zhang, F. Du, S. Xue, H. Cheng, X. Zhang, R. Song, and Y. Li. Design and modeling of a bio-inspired compound continuum robot for minimally invasive surgery. *Machines*, 10(6):468, 2022.

[48] W. Ba, X. Dong, A. Mohammad, M. Wang, D. Axinte, and A. Norton. Design and validation of a novel fuzzy-logic-based static feedback controller for tendon-driven continuum robots. *IEEE/ASME Transactions on Mechatronics*, 26(6):3010–3021, 2021.

[49] M. Tummers, V. Lebastard, F. Boyer, J. Troccaz, B. Rosa, and M. T. Chikhaoui. Cosserat rod modeling of continuum robots from newtonian and lagrangian perspectives. *IEEE Transactions on Robotics*, 39(3):2360–2378, 2023.

[50] J. L. Chien, L. T. L. Clarissa, J. Liu, J. Low, and S. Foong. Kinematic model predictive control for a novel tethered aerial cable-driven continuum robot. In *Proceedings of the IEEE/ASME International Conference on Advanced Intelligent Mechatronics (AIM)*, pages 1348–1354. IEEE, 2021.

[51] Y. Li, D. H. Myszka, and A. Murray. The kinematics of constant curvature continuum robots through three segments. *IEEE Robotics and Automation Letters*, 2023.

[52] M. Ay. Modeling and analysis of a modular-structured tendon-driven continuum robot for the three-dimensional end effector coordinate. *Simulation Modelling Practice and Theory*, 127:102787, 2023.

[53] G. Fang, X. Wang, K. Wang, K.-H. Lee, J. D. Ho, H.-C. Fu, D. K. C. Fu, and K.-W. Kwok. Vision-based online learning kinematic control for soft robots using local gaussian process regression. *IEEE Robotics and Automation Letters*, 4(2):1194–1201, 2019.

[54] A. Bicchi, F. Fati, M. Quacquarelli, E. Votta, and E. De Momi. Optimizing heart valve surgery with model-free catheter control. In *Proceedings of the Hamlyn Symposium on Medical Robotics*, 2023.

[55] A. Parvaresh and S. A. A. Moosavian. Dynamics and path tracking of continuum robotic arms using data-driven identification tools. *Robotica*, 40(4):1098–1124, 2022.

[56] A. Tariverdi, V. K. Venkiteswaran, M. Richter, O. J. Elle, J. Tørresen, K. Mathiassen, S. Misra, and Ø. G. Martinsen. A recurrent neural network-based real-time dynamic model for soft continuum manipulators. *Frontiers in Robotics and AI*, 8:631303, 2021.

[57] V. Klema and A. Laub. The singular value decomposition: Its computation and some applications. *IEEE Transactions on Automatic Control*, 25(2):164–176, 1980.

[58] Xiu Zhang, Izadyar Tamadon, Benjamín Ignacio Fortuño Jara, Vanessa Cannizzaro, Angela Peloso, Anna Bicchi, Andrea Aliverti, Emiliano Votta, Arianna Menciassi, and Elena De Momi. Design and hysteresis compensation of a telerobotic system for transesophageal echocardiography. *IEEE Robotics and Automation Letters*, 10(1):104–111, 2025.

[59] Angela Peloso, Nadia D'Alessandro, Xiu Zhang, Arianna Menciassi, and Elena De Momi. A robotic system with path planning and visual guidance for teleoperated left atrial appendage closure. *IEEE Robotics and Automation Letters*, 10(9):9304–9311, 2025.

[60] You Yue, Wang Hao, Hao Guanjie, and Yao Yao. Uuv target tracking path planning algorithm based on deep reinforcement learning. In *2023 8th Asia-Pacific Conference on Intelligent Robot Systems (ACIRS)*, pages 65–71, 2023.

[61] Mirko Leomanni, Gianni Bianchini, Andrea Garulli, and Renato Quartullo. Sum-of-norms periodic model predictive control for space rendezvous. *IEEE Transactions on Control Systems Technology*, 30(3):1311–1318, 2022.

[62] Mirko Leomanni, Gianni Bianchini, Andrea Garulli, and Renato Quartullo. Sum-of-norms periodic model predictive control for space rendezvous. *IEEE Transactions on Control Systems Technology*, 30(3):1311–1318, 2022.

[63] Linnea Persson and Bo Wahlberg. Variable prediction horizon control for cooperative landing on moving target. In *2021 IEEE Aerospace Conference (50100)*, pages 1–10, 2021.

[64] Keunjun Choi, Jaewoon Kwon, Taeyoon Lee, Changwoo Park, Jinwon Pyo, Choongin Lee, SungPyo Lee, Inhyeok Kim, Sangok Seok, Yong-Jae Kim, and Frank Chongwoo Park. A hybrid dynamic model for the ambidex tendon-driven manipulator. *Mechatronics*, 69:102398, 2020.

[65] Yilun Sun, Yuqing Liu, Ying Su, and Tim C. Lueth. Model predictive control of 2-dof tendon-driven continuum robot using optical tracking. In *2024 IEEE International Conference on Advanced Intelligent Mechatronics (AIM)*, pages 1278–1283, 2024.

[66] Maximillian Hachen, Chengnan Shentu, Sven Lilge, and Jessica Burgner-Kahrs. A non-linear model predictive task-space controller satisfying shape constraints for tendon-driven continuum robots, 2024.

[67] Julian Berberich and Frank Allgöwer. An overview of systems-theoretic guarantees in data-driven model predictive control. *Annual Review of Control, Robotics, and Autonomous Systems*, 8(1):77–100, May 2025.

[68] Anna Bicchi, Xiu Zhang, Benjamín Ignacio Fortuño Jara, Vanessa Cannizzaro, Angela Peloso, and Elena De Momi. Model-based position control of a tendon-driven variable-length continuum robot for minimally invasive mitral valve repair. *IEEE Transactions on Medical Robotics and Bionics*, 7(2):562–571, 2025.

[69] Wang et al. Normal reference values for mitral annular plane systolic excursion by motion-mode and speckle tracking echocardiography: a prospective, multicentre, population-based study. *European Heart Journal - Cardiovascular Imaging*, 24(10):1384–1393, 08 2023.

[70] Chuanchuan Pan, Zhen Deng, Chao Zeng, Bingwei He, and Jianwei Zhang. Optimal visual control of tendon-sheath-driven continuum robots with robust jacobian estimation in confined environments. *Mechatronics*, 104:103260, 2024.

[71] Tingshu Hu and Zongli Lin. Composite quadratic lyapunov functions for constrained control systems. *IEEE Transactions on Automatic Control*, 48(3):440–450, 2003.

[72] Chuanchuan Pan, Zhen Deng, Chao Zeng, Bingwei He, and Jianwei Zhang. Optimal visual control of tendon-sheath-driven continuum robots with robust jacobian estimation in confined environments. *Mechatronics*, 104:103260, 2024.

[73] David Ouyang, Bryan He, Amirata Ghorbani, Neal Yuan, Joseph Ebinger, Curtis P Langlotz, Paul A Heidenreich, Robert A Harrington, David H Liang, Euan A Ashley, et al. Video-based ai for beat-to-beat assessment of cardiac function. *Nature*, 580(7802):252–256, 2020.

Abstract in lingua italiana

La riparazione transcatetere della valvola mitrale richiede un raggiungimento accurato di strutture anatomiche soggette a significative dinamiche fisiologiche, mettendo in crisi strategie di controllo convenzionali basate su ipotesi statiche. Questo lavoro presenta un framework di controllo predittivo per il raggiungimento di obiettivi dinamici mediante cateteri robotici continui azionati mediante tendini.
Il moto dell' obittivo viene modellato e predetto online, mentre uno schema di Model Predictive Trajectory Planning (MPTP) genera traiettorie anticipative verso la valvola in movimento. Per gestire il comportamento non lineare e dipendente dalla configurazione, tipico dei robot continui, viene integrata nell' anello di controllo una strategia di adattamento online del Jacobiano, arricchita da un meccanismo di rilevazione della dead-zone e dalla gestione della saturazione dei motori, al fine di garantire stabilità in presenza di vincoli attuativi.
L'approccio è validato su una piattaforma sperimentale dedicata, composta da un robot continuo azionato a tendini e da uno stadio di movimento in grado di riprodurre dinamiche valvolari fisiologicamente ispirate. I risultati mostrano un tasso di successo del 100%, superiore rispetto a Controllo basato Modello Predittivo classico (55%) e un controllore Proporzionale-Integrale-Derivativo basato su modello analitico (75%). Il metodo proposto consente traiettorie più brevi (72 $\pm$ 6 mm) e una riduzione del tempo di raggiungimento dell' obiettivo (260 $\pm$ 45 s), mantenendo robustezza rispetto a variazioni di ampiezza e frequenza del moto.
Tali risultati evidenziano l'efficacia dell'integrazione tra pianificazione predittiva e adattamento cinematico online per interventi robotici su obiettivi anatomici dinamici.

Parole chiave: Riparazione transcatetere autonoma della valvola mitrale, Pianificazione predittiva della traiettoria basata su modello, Targeting dinamico della valvola mitrale, Aggiornamento online del Jacobiano

Acknowledgements

I would like to thank my family for all the support they have given me throughout my entire academic journey and for standing by me during the hardest moments. I am deeply grateful to my girlfriend, Sofia, for her patience when I dedicated too much time to my work and for her constant affection.
I would also like to thank my friends in Parma. Although I am not able to see them very often, I truly value the time we spend together having fun. Finally, I would like to thank my coursemates. I prefer calling them mates rather than colleagues, because we have shared much more than just studying at university.
Lastly, I would like to thank everyone in the laboratory for giving me the opportunity to work not as a guest, but as a member of the research team. In particular, I would like to thank my co-advisor, Anna Bicchi, for the time she dedicated to discussing my ideas (even when they were stupid) and for her patience.